Doctoral Dissertations   Graduate School

12-2017

Low Energy Recoil Simulations in MgO, LiNbO3, and LiTaO3 Using *Ab Initio* Molecular Dynamics

Benjamin Aaron Petersen
University of Tennessee, Knoxville, bpeters7@utk.edu

Follow this and additional works at: https://trace.tennessee.edu/utk_graddiss

Part of the Ceramic Materials Commons, and the Semiconductor and Optical Materials Commons

To the Graduate Council:

I am submitting herewith a dissertation written by Benjamin Aaron Petersen entitled "Low Energy Recoil Simulations in MgO, LiNbO3, and LiTaO3 Using *Ab Initio* Molecular Dynamics." I have examined the final electronic copy of this dissertation for form and content and recommend that it be accepted in partial fulfillment of the requirements for the degree of Doctor of Philosophy, with a major in Materials Science and Engineering.

Yanwen Zhang, Major Professor

We have read this dissertation and recommend its acceptance:

William J. Weber, Maik K. Lang, Yanfei Gao

Accepted for the Council:

Dixie L. Thompson

Vice Provost and Dean of the Graduate School

(Original signatures are on file with official student records.)

Low Energy Recoil Simulations in MgO, LiNbO3, and LiTaO3 Using *Ab Initio* Molecular Dynamics

A Dissertation Presented for the

Doctor of Philosophy

Degree

The University of Tennessee, Knoxville

Benjamin Aaron Petersen

December 2017

Dedicated to my Mother Debora Petersen and Brother Jeremy Petersen

Acknowledgments

I would like to thank my mother Debora Petersen and brother Jeremy Petersenfor their help and support during my education.

I would also like to thank my research colleagues, Chris Ostrouchov, Bin Liu, Miguel Crespillo, and Jianqi Xi, in addition to my advisors Yanwen Zhang and Bill Weber for their input and discussions while working on the work presented here.

Abstract

Ab initio molecular dynamics (AIMD) was utilized to test a series of materials, MgO, LiNbO$_3$, and LiTaO$_3$, to determine defect structures produced due to low energy recoil events . The kinetic energy required to displace an atom from its lattice site, the threshold displacement energy, was calculated for an array of directions in each material, based on symmetry and complexity of the structure. MgO having a simple rock salt structure provided a model material for demonstrating computational techniques used later on LiTaO$_3$ and LiNbO$_3$. The minimum values for displacing an atom were at 25.5 eV for O and 29.5 eV for Mg. For LiNbO$_3$ and LiTaO$_3$, the minimum energy for displacing an atom was 6 eV for Li in LiTaO$_3$ and 14 eV for Li in LiNbO$_3$. Average values for threshold displacement energies agreed well with those used in calculations, but they have not yet been accurately measured experimentally. Additionally, the defect structures and properties were identified and reported as a result of the simulations. The high defect formation energy reported for cation vacancies means that they are unstable in the structure and will either recombine, form defect complexes, or migrate to defect sinks in the material.

Table of Contents

List of Tables

List of Figures

Chapter 1

Introduction

1.1 Purpose

Exploring radiation damage in materials, especially at small scales where primary damage events happen is very challenging. The focus of this research is to utilize modern computational techniques from molecular dynamics and density functional theory to determine the defect properties in various oxide materials as produced through irradiation. The creation of point defects during radiation damage happens incredibly quickly (on the order of 10^{-13}s) such that gathering information on these defects via experimental observation is difficult if not impossible. Therefore, with the tools available to us currently, the only way to gather information about these processes is by simulating these events. Simple oxides like MgO fare well when performing simulations due to their simple ionic and electronic structures. More complex ternary oxides can be more difficult to simulation utilizing classical techniques. Ternary oxides like $LiNbO_3$ and $LiTaO_3$ for example are poorly suited to study by classical molecular dynamics so to properly study them, we need to use more computationally intensive methods like density functional theory in combination with molecular dynamics. When combining these tools on short time scales, it is then possible to analyze the radiation response of a material at very small length scales. The work presented here is intended to bridge the gap between current experimental observations and reported results from prior density functional theory based calculations.

The dynamic nature of the calculations to be performed require extra care due to any number of limitations imposed by the computational methodologies currently employed, which will be discussed and considered. Modern standards in computational materials science require rigorous testing of the simulation parameters before proper simulations can commence which will also be explored. Before any simulation takes place, an understanding of the radiation damage event is required to explain the reasoning behind simulation decisions. Then a sampling of material properties is required to ensure accurate representation of the physics involved. After all of these properties have been verified and the simulation parameters tested, then finally simulations relating to the radiation damage event can begin. Finally, after all defect structures are cataloged, the properties of the defects can be calculated and conclusions can be drawn regarding the material response under irradiation.

1.2 Radiation damage

1.2.1 Introduction to radiation damage

When an energetic particles, be it an ion, electron, neutron, photon, or any other atomic or subatomic particles, interact with a material, there are several steps that can describe the various time and interaction scales throughout the course of the event. Gary S. Was [8] describes the radiation damage event in six basic steps, illustrated in figure 1.1.

1. Interaction of an energetic incident particle with a lattice atom (figure 1.1a)

2. Transfer of kinetic energy to the lattice atom which creates a primary knock-on atom (PKA) (figure 1.1b)

3. Displacement of the PKA from its lattice site (figure 1.1c)

4. Passage of the displaced atom through the lattice and subsequent creation of additional knock-on atoms (figure 1.1d)

5. Production of a displacement cascade (a collection of point defects produced by the PKA) (figure 1.1e)

6. Termination of the PKA in the lattice (as either an interstitial, replacement, or at a sink for defects) (figure 1.1f)

$$R = N \int_{E_{min}}^{E_{max}} \int_{T_{min}}^{T_{max}} \phi(E_i)\sigma(E_i, T)\nu(T)dTdE_i \qquad (1.1)$$

Radiation damage is described by equation 1.1 [8] where R is the number of displacements per unit volume, N is the atom number density, E_{min} and E_{max} are the minimum and maximum energy of particle, T_{min} and T_{max} are the minimum and maximum energy transferred in a collision of a particle energy E_i and lattice atom, $\sigma(E_i, T)$ is the cross section for the collision resulting in transfer of energy T, and finally $\nu(T)$ is the number of displacements per PKA. Determining the value of $\nu(T)$ can be done with several models, like the Kinchin-Pease model. This model requires knowledge of the minimum value of kinetic energy required to displace an atom from its initial lattice site and produce a Frenkel pair [9]. This value is known as the threshold displacement energy or E_d . Codes that estimate radiation damage, like TRIM (Transmission of Ions in Matter)[10] require E_d as an input parameter when estimating damage as well.

As the atom progresses through the lattice, it will lose energy to the electrons of the system (electronic energy loss) and through collisions with nuclei in the system (nuclear energy loss). At higher energies, the incident particle will lose energy mostly due to electronic effects. After it loses enough energy however, it will begin to interact with the nuclei of the target system. These nuclear collisions are where the threshold displacement energy plays an important role in estimating the damage, depth, and distribution of defects in a material under irradiation.

Being as the threshold displacement events occur at the very minimum energy required for displacing an atom, it is key to understanding which defects are produced at the end of the cascade. Codes and models estimate damage based on E_d , but the actual type of defects that occur in the material can affect the structural evolution of the material[8]. Some types of defects will not be easy to detect (replacements, some types of antisite defects) while others like dislocation loops,

color centers produced from vacancies, bubbles and voids are easier to detect. Some effects of radiation damage are even visible to the naked eye like color changes due to defects produced.

1.2.2 Energetic particle interaction with solid matter
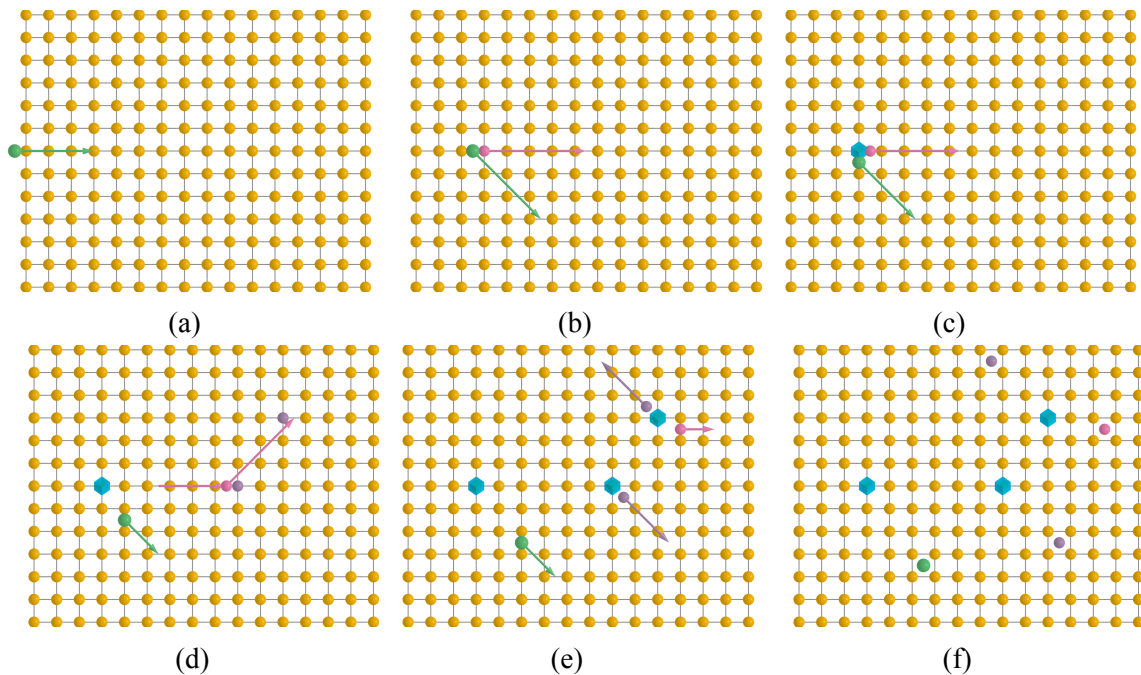
Figure 1.1: Schematic representation of the steps in a radiation damage event. Lattice atoms are orange, the incident particle is green, the PKA is pink, additional knock on atoms are purple and the vacancies are shown in blue.

From figure 1.2, the shortest time scale interactions in radiation damage are related to the primary damage production. This is the portion of radiation damage described in figure 1.1. Beyond this time and length scale, larger more easily observed reactions happen like defect mobility, void and bubble formation, and recombination. The mobility of defects also allows for the production of larger defects like dislocation loops. Large defects in the structure begin to affect the macroscopic properties like mechanical properties. Dislocations and point defects further affect the motion of dislocations in the material affecting how the material can deform. Swelling (due to void and bubble formation in addition to dislocation and point defect production) also affects how the mechanical properties change, especially if the material is required to be a certain size and shape.
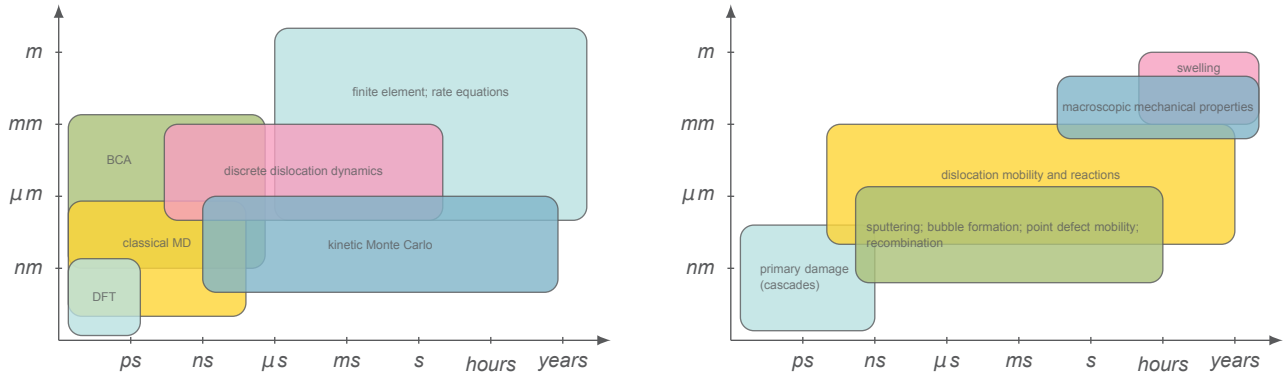
Figure 1.2: Various time and length domains for multiscale materials science modeling in relation to radiation damage affects taken from Freyss [1] and modified slightly (increased the length of BCA (binary collision approximation) region).

As a compliment to experimental observations, simulations can fill in the gaps of observable events with finer time and resolution scales. Figure 1.2 on the lower portion shows the overlap and differences between the various techniques used to simulate materials under irradiation. Especially at the fine time and length scales there are a variety of tools available. Some of these tools require additional knowledge. For instance, classical molecular dynamics requires a well defined function or potential to represent atomic interactions. The interactions can be quite complex and the equations to represent these events can fail to provide a complete picture of what is happening in the material. Things like charge transfer, evolving oxidation states, and multiple component systems all require consideration for accurate simulations. When there are too many of these interactions and terms to consider, many of the models for classical MD potentials cannot predict properties of their representative systems.

A one component system, a pure copper crystal for example, is one of the first materials simulated under irradiation[11]. There was only one term really required to describe the interaction between atoms– a Cu-Cu interaction term. When two component systems exist, there are three terms at minimum required to describe the behavior. For instance, in MgO, there is an Mg-Mg term, an O-O term, and an Mg-O term required. For a three component oxide, like $LiNbO_3$, there would be at minimum six components to the potential– Li-Li, Li-Nb, Li-O, Nb-Nb, Nb-O, and O-O. This neglects other oxidation states (like Nb can have in oxide materials) and other longer

5

range interactions. A four component system is yet again more complex.

1.3 Material selection

When selecting materials for analysis, especially for relatively new techniques, it is advantageous to select a material that is well studied and simple to analyze. If looking at materials purely from their ease of simulation, then a very good candidate material would be MgO since it is used as a standard reference material for several density functional theory (DFT) codes. In addition to being well studied with DFT it has had well developed classical MD potentials for running simulations. Additionally, the MD potentials for MgO are simple compared to more complex oxides since they typically only need to describe three interactions– Mg-Mg, O-O, and Mg-O [12]. When more components are added to the system, mutli-component interactions become much more complex. To further add to the difficulty in simulation, charge must be considered. MgO potentials just consider one charge state for Mg and one charge state for O. The simulations become more difficult once more charge states can be considered.

After verifying procedures and methodology produce believable results, more challenging materials can be selected. In this case, two ABO_3 oxides are of particular interest due to their properties under irradiation and lack of classical MD potentials that can simulate these conditions. In particular, the heavy cations in $LiNbO_3$ and $LiTaO_3$ can exist in multiple charge states. At ground state in those materials, the cations exist at a +5 charge state, but they can exist at +4, +3, and +2 in $LiNbO_3$ or $LiTaO_3$ defects in addition to other materials[13, 14]. Unless a potential can take into account the local geometry and the effects on the charge state of the atom, classical MD can fail to predict the behavior of defect structures.

$LiNbO_3$ and $LiTaO_3$ exhibit desirable properties for use in optical applications, but their main drawback is that they become damaged under intense optical radiation and lose their properties that make them useful[15, 16]. One of the main ways to stabilize the damage is with the inclusion of Mg

in the form of MgO. All three of the materials presented here, LiTaO$_3$, LiNbO$_3$, and MgO therefore are useful in the same application– wave guides and radiation resistance in those materials.

1.3.1   MgO
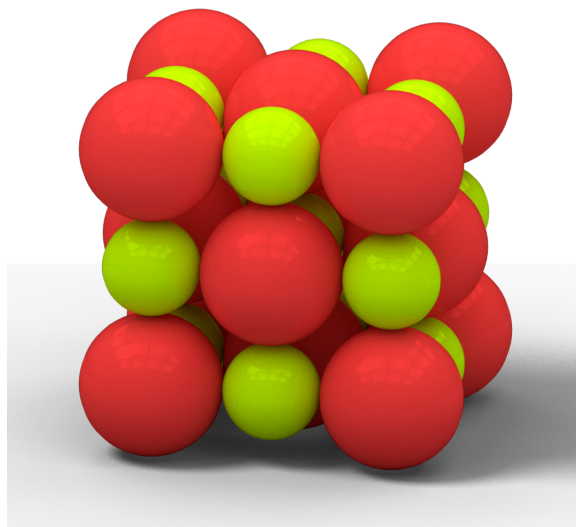
Figure 1.3: Cubic MgO unit cell. O atoms are red; Mg are green (all colors in atomic models in this work are taken from their colors in Jmol[2])

Figure 1.3 shows the unit cell for MgO. It has the rocksalt crystal structure (space group Fm$\bar{3}$m, no. 225) which consists of two interpenetrating FCC lattices of Mg and O ions. It is usually a white, odorless powder (clear single crystals are available) with a high melting point (2852°C) and is chemically inert. Historically, MgO was known as magnesia alba (white mineral from magnesia). Due to its simple crystal structure, MgO has long been used as a material for testing both experimental techniques and theoretical models. It has been widely used as a substrate material for studying the vibrational properties of crystals due to its stability.

Perhaps its most common use currently is as a refractory material since it has a high melting point and is chemically stable at high temperatures. Additionally, it has a high thermal and low electrical conductivity making it very widely used in refractory applications as well as fireproofing. One of the other primary uses for MgO is in areas where it acts as an acid buffer and stabilizer for dissolved heavy metals. Most metals are more soluble in water at low or high pH. Solubility in

7

turn affects the bioavailability of the dissolved metals as well as their mobility through soil and groundwater systems. MgO is often used when it is imperative to ensure heavy metals do not enter these systems since it can both change the acidity and precipitate dissolved heavy metals.

One of the many uses of MgO is as a material for packing around and stabilizing nuclear waste products. For instance, at the Waste Isolation Pilot Plant, where radioactive waste and materials are stored for long term isolation, MgO is the preferred material for packing around containers. Dissolved heavy metals will be stabilized in MgO thus preventing contamination of ground water with radioactive material should any escape containment over their long decay process. The low chemical activity, resistance to radiation damage, and low cost make it an ideal material for long term waste storage[17].

In addition to storing and protecting nuclear waste, MgO has also been investigated as a matrix for inert matrix nuclear fuels and as a matrix for the transmutation of fission byproducts[17]. Understanding the radiation response of MgO has been researched since the 1950's. The process by which point defects form is integral to the current knowledge of behavior of the material in radioactive environments, which is the focus of current research.

1.3.2 $LiNbO_3$ and $LiTaO_3$

$LiNbO_3$ and $LiTaO_3$ have a combination of desirable qualities (ferroelectric, piezoelectric, photoelasticity, and nonlinear optical polarizability) that arise from their crystal structure. They are both in the trigonal crystal system (R3c) that lacks inversion symmetry compared to the similar ilmenite crystal structure of higher temperature $LiNbO_3$. As shown in figure 1.4, the unit conventional unit cell for $LiNbO_3$ ($LiTaO_3$ has the same structure) contains alternating layers of anions and cations. There has been a great deal of interest in the higher temperature structure of the material as it has higher symmetry[14, 18, 19], but that is not the focus of this work.

The theoretical and measured lattice parameters of both $LiNbO_3$ and $LiTaO_3$ are nearly identical; the only major difference in the two structures is with the weight of the second cation in
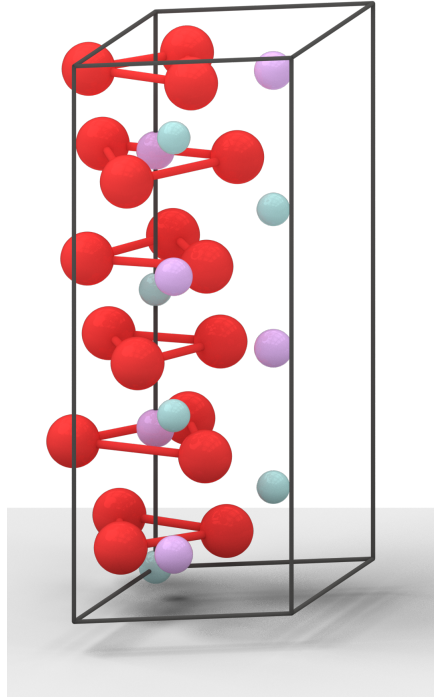
Figure 1.4: Hexagonal LiNbO$_3$ unit cell. O atoms are red; Li atoms are purple; Nb atoms are teal. Octahedra of oxygen atoms contained within the unit cell are highlighted. Nb atoms sit at the center of these sites.

the structure. The heavy cation in the material, Nb and Ta are in the same column on the periodic table. They have the same valence electron configuration when in the +5 oxidation state, but at different orbitals. Their masses however are considerably different with Nb weighing 92.906 u and Ta weighing nearly double that at 180.948 u.

The primary interest in LiNbO$_3$ and LiTaO$_3$ has been for their non-linear optical properties. They are typically used as wave guides for light. Of even more recent interest has efforts to utilize mixtures of LiNbO$_3$ and LiTaO$_3$ along with dopants like MgO to prevent optical radiation from damaging the crystals in their primary applications.

Historically, several tests have been done to analyze the low energy radiation response of both LiNbO$_3$ and LiTaO$_3$ but the results proved to be inconclusive. The chosen method of analysis in those experiments was to look at the color centers produced after irradiation and see how they

evolved over time. There were, however, two major difficulties surrounding this. The first is that only recently have high quality stoichiometric crystals become available and the second is that the color centers produced by O^{2-} vacancies obscure the signals from other defects[20]. The crystals available at the time were riddled with intrinsic defects and oxygen vacancies are relatively easy to form at room temperature due to the growth conditions of the crystals. Effectively, this makes it nearly impossible to gauge the formation of cation defects in these two materials since both are easily obscured by intrinsic defects and those produced from anion defects.

Under irradiation, $LiNbO_3$ and $LiTaO_3$ exhibit the formation of amorphous ion tracks[21, 22]. Partly this is due to the phase stability and growth conditions of the crystal; if the $LiNbO_3$ phase is not completely stoichiometric and there is an appreciable concentration of intrinsic defects, these intrinsic defects can play a role in the amorphization of the material[20, 22].

$LiNbO_3$ provides a good system for ion track formation and amorphization in ceramic oxide materials. The ease with which it forms amorphous regions allows for lower energy experiments to study these phenomena. Additionally, amorphization and ion tracks can be used as a processing method to produce nano scale structures in the material with lower incident particle energy. Predamage in $LiNbO_3$ has been shown to facilitate the formation of ion tracks as well suggesting a synergistic effect of accumulated damage in $LiNbO_3$.

More work has been carried out on $LiNbO_3$ currently than on $LiTaO_3$ because of the availability of high quality $LiNbO_3$ crystals. Only recently have more high quality $LiTaO_3$ crystals become available compared to commercially available $LiNbO_3$ crystals. Both are grown through the Czochralski process where seed crystal is grown to a much larger single crystal of the same material.

Chapter 2

Computational and theoretical background

2.1 Molecular dynamics

2.1.1 Historical context

Table 2.1: Timeline of the major advances in molecular dynamics and statistical mechanics

year	work	authors
1953	"Equation of state calculations by fast computing machines" [23]	Metropolis et al
1955	"Fermi, Pasta, and Ulam Los Alamos report"[24]	Fermi, Pasta, and Ulam
1956	"Phase Transitions for a Hard Sphere System" [25]	Alder and Wainwright
1960	"Dynamics of Radiation Damage"[11]	the Vineyard group
1964	"Correlations in the Motion of Atoms in Liquid Argon"[26]	Rahman
1971	"Molecular Dynamics Study of Liquid Water"[27]	Rahman and Stillinger
1972	"NpT-ensemble Monte Carlo calculations for binary liquid mixtures"[28]	McDonald
1980	"Molecular dynamics simulations at constant pressure and/or temperature"[29]	Andersen
1980	"Crystal Structure and Pair Potentials: A Molecular-Dynamics Study"[30]	Parrinello and Rahman
1981	"Polymorphic transitions in single crystals: a new molecular dynamics method"[31]	Parrinello and Rahman
1985	"Unified approach for Molecular Dynamics and Density-Functional Theory"[32]	Car and Parrinello

One of the key tools developed since the 1950s for understanding atomic behavior is molecular dynamics. MD makes several assumptions about the materials being simulated, one of them being the hard sphere model. Early Monte Carlo methods describe this approach. Another key assumption is that the forces between atoms can be represented as infinite springs or force fields. The model for this interatomic interaction is called a potential. Table 2.1 shows a basic timeline of the major advances in molecular dynamics and atomic simulation.

Early on, in the 1960's, simple physical models based on hard spheres (rubber balls) connected with sticks were used. Even today, the dynamics of crystals are studied with charged particles to represent atoms. Perhaps the earliest calculations that would later become molecular dynamics were those of Metropolis et al in 1953. Metropolis Monte Carlo was developed to take advantage of the advances in computational power available at the time to numerically analyze a liquid of two dimensional spheres[24]. Expanding on this early Monte Carlo simulation technique was the work done by Fermi, Pasta, and Ulam (and Tsingou) (FPU) in 1955 and later. FPU developed their model based on one dimensional crystals. Their result was an apparent paradox, known as the FPU problem. This experiment was key in showing the complexity of nonlinear behavior and the value of computer simulations to analyze systems.

Perhaps most relevant to the work presented here is the 1960 paper "Dynamics of Radiation Damage" by the Vineyard group at Brookhaven Lab. In it, Gibson simulated radiation damage events up to 400 eV in a metallic copper system. Their work was the first instance of utilizing a classical MD approach to analyzing radiation damage in a crystalline material. In their case, they employed a Born-Mayer potential to describe the repulsive force between atoms in addition to a cohesive surface force. The methodology employed in that simulation is very similar to that employed today for calculating threshold displacement energies[11]. In 1964, Rahman published his work on the simulation of liquid Ar using a Lennard-Jones potential. Since the Lennard-Jones potential describes the interatomic interaction of inert particles (noble gases), calculation of system properties from these efforts compared well with experimental data[26].

In the early 1970's, there were advances in computational techniques allowing for the use of more ensembles to describe molecular systems. However, it was not until the 1980's that major work by Andersen and later Parrinello and Rahman created frameworks for utilizing ensembles[30]. The last major relevant advance in molecular dynamics came about in 1985 with the work by Car and Parrinello. Their work combined DFT and MD[32]. While this work does not use Car-Parrinello molecular dynamics, it is important to note that it is a major advance in computational physics and materials science to combine the two techniques. The rest of this work utilizes simpler Born-Oppenheimer based molecular dynamics instead.

2.1.2 Classical molecular dynamics algorithm
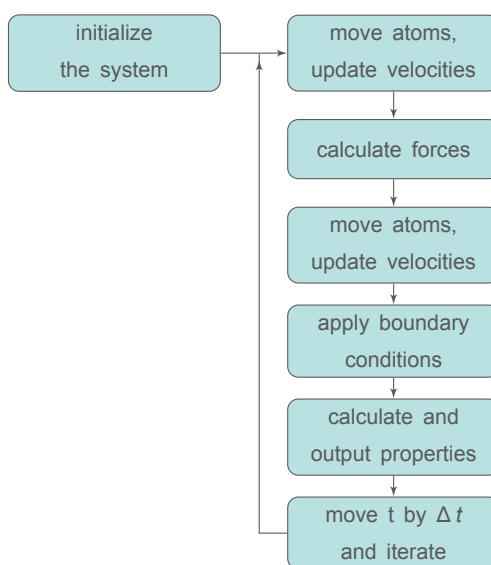
Figure 2.1: Basic flow chart for the molecular dynamics algorithm.

Figure 2.1 shows the basic steps needed for a classical molecular dynamics simulation. First the system is initialized (given an initial position, velocity, acceleration, charge, etc. for each atom). Then the atoms are moved based on the calculated interatomic forces. The velocities are updated and new forces calculated. Then the atoms are moved again and boundary conditions applied. Output properties can then be calculated from this system based on the type of boundary conditions and input parameters. Finally, time is progressed forward by a selected interval and

the process can move forward. Selecting the time step is important because if it is too large, the integration of system properties does not converge. This is usually obvious, but testing the system with smaller time steps ensures that the selected time step is adequate[33].

At the "apply boundary conditions" step in figure 2.1, the boundaries and constraints are applied to the system. These boundaries are used to isolate certain properties of the system and ensure certain thermodynamic properties are conserved. The table 2.2 shows five of the main options when considering these boundaries. In addition to bounds on the properties and configuration of the system, the edges of the simulation can be taken into account[33]. For instance, all of the work presented here employs a periodic boundary condition (all boundaries on the simulation cell are treated as periodic).

Table 2.2: Choices of ensembles and the properties that are kept constant in each. Alternative names are also shown.

ensemble	other names	terms
NVE	microcanonical	N (number of particles), V (volume), E (energy)
NVT	caonical	N (number of particles), V (volume), T (absolute temperature)
μVT	grand canonical	μ (chemical potential), V (volume), T (absolute temperature)
NPH	isoenthalpic-isobaric	N (number of particles), P (pressure), H (enthalpy)
NPT	isothermal-isobaric	N (number of particles), P (pressure) T (absolute temperature)

2.2   Density functional theory

The basis of density functional theory (DFT) is that all of the properties of a system can be generated from the electron density[34]. The name, density functional theory, comes from the assumption that the properties of a material can be determined by functionals (a function of another function) of the electron density. The algorithm works by taking an initial guess of the electron density and following an iterative process that produces self consistent results. Once the input and outputs of the algorithm approach values within a specified tolerance, the result can be returned along with other calculated properties from that result. A simplified flow chart of this process is shown in figure 2.2.

2.2.1 Historical context

Table 2.3: Timeline of the relevant major advances in quantum chemistry and density functional theory.

year	work	author
1927	Hartree self-consistent field (SCF) methods[35]	Hartree
1951	Slater method for simplifying Hatree-Fock method[36]	Slater
1952	First application of Slater's method[37]	Pratt
1964	"Inhomogeneous Electron Gas"[38]	Hohenberg and Kohn
1965	One electron exchange and correlation [39]	Kohn and Sham
1966	First use of Kohn-Sham equations with an LDA pseudopotential[40]	Tong and Sham
1985	"Unified approach for Molecular Dynamics and Density-Functional Theory"[32]	Car and Parrinello

Table 2.3 shows a timeline of the major events in the development of DFT. The first major development was the Hartree self-consistent field (SCF) method in 1927; these methods were used to describe approximations of wave functions and energies for ions. Hartree sought to solve the many body time independent Schroedinger equation from fundamental principles alone. Later on this method was expanded by Fock as Hartree's original approximation neglected the asymmetry of the wave function. Later on, in the 1950's, further simplification of the Hartree-Fock methods were discovered and implemented. However, it was not until the 1960's with the methods from Hohenberg, Kohn, and Sham that the foundations for modern DFT were codified. In the 1980's Car and Parrinello began work on unifying approaches to MD and DFT by adding additional degrees of freedom to classical MD based on DFT. Only more recently (since the 2000's) has it become feasible to simulate larger systems due to the increased availability of computational power.

2.2.2 Density functional theory algorithm

To simplify calculations, the first approximation used is the Born-Oppenheimer approximation. This holds that the electron and nuclear motion can be decoupled from one another because the electrons move much more rapidly than the nuclei[41]. The nuclei are treated as being fixed during electronic structure calculations. The electron density, $n(\mathbf{r})$, is defined such that $n(\mathbf{r})d^3r$ is the probability of finding an electron in the volume d^3 about $\mathbf{r}$ [34]. For a single electron, it is $|\phi_i(\mathbf{r})|^2$
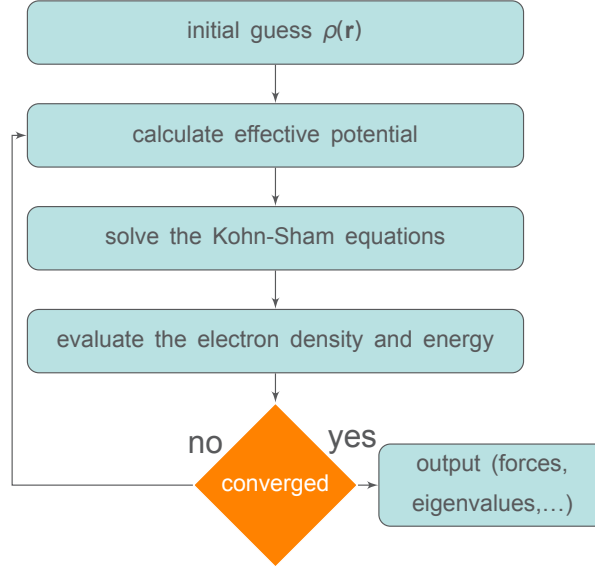
Figure 2.2: Basic flow chart for the density functional theory algorithm.

where $\phi_i(\mathbf{r})$ is the single electron wave function.

$$\rho(\mathbf{r}) = \sum_i^N |\phi_i(\mathbf{r})|^2 \tag{2.1}$$

The first step in calculating properties from the DFT algorithm is to have an initial guess of the electron density $\rho(\mathbf{r})$, shown in equation 2.1. $\rho(\mathbf{r})$ is determined as the summation of the probability of finding an electron based on each wave function, $\phi_i(\mathbf{r})$.

$$v_{eff}(\mathbf{r}) = V_{en}(\mathbf{r}) + \int \frac{\rho(\mathbf{r'})}{|r - r'|} d\mathbf{r'} + V_{xc}[\rho(\mathbf{r})] \tag{2.2}$$

The effective potential in 2.2 is given as a function of both the electron density and the exchange-correlation terms, V_{xc}. There are many ways to describe the exchange-correlation term in the system and it is typically broken up into two parts– the exchange and correlation. Solving for v_{eff} allows it to be input into a wave equation where.

$$\left[-\frac{\hbar^2}{2m_e} + v_{eff} \right] \Psi_i = \varepsilon_i \Psi_i \tag{2.3}$$

16

Solving the eigenvalue problem in 2.3 yields a new wave function which can then be used to determine a new electron density.

$$\rho(\mathbf{r}) = \sum_i |\Psi_i(r)|^2 \rightarrow E_{total}[\rho(\mathbf{r})] = \dots \tag{2.4}$$

After calculating the new electron density from equation 2.4, the result is compared with the electron density from the first step. If they are within whatever convergence criteria set at the start of the calculation, the result and final properties can be computed and reported. Among these properties are the forces, pressure, total energy, eigenvalues of the wave equation, and more depending on the parameters of the code and type of calculation.

Table 2.4: Basic comparison of the types of basis sets for commonly used DFT codes

code	basis set
VASP	Plane wave (PW)[42]
SIESTA	LCAO (linear combination of atomic orbitals)[43]
ABINIT	PW[44]
CASTEP	PW[45]
Quantum ESPRESSO	PW[46]
WIEN2K	LAPW (linearized augmented plane wave) + LO (local orbital) [47]

2.2.3 Pseudopotentials

When using the SIESTA code, there are extra steps involved with configuring the inputs, namely the generation of suitable pseudopotentials. A pseudopotential, shown schematically in figure 2.3, is the potential used to produce a wave function similar to the wave function produced by an actual atomic potential. The benefit of using a pseudopotential, (introduced by Hans Hellmann in 1934) is that it is a simpler shape and the resulting wave function is easier to work with. The pseudopotential is constructed such that the all-electron (or full-potential) core states are eliminated. The main benefit of this is the description of the valence electrons is much simpler mathematically (fewer

Forier modes), which makes using plane wave and other basis sets feasible. In this case, the core electrons are treated as frozen (they are considered to be together with the nuclei as the rigid ion core) such that the valence electrons are the only ones considered explicitly. SIESTA also contains an auxiliary code for generating pseudopotentials. The input consists of the atom, mass, orbital configuration, and occupation.
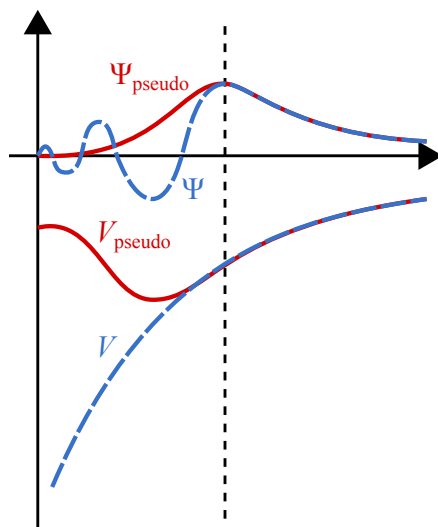
Figure 2.3: Schematic representation of the wave function and potential of an atomic potential and a pseduopotential [3].

There are many ways to describe a pseudopotentials and many different approximations that are available to the user. Since testing the applicability of chosen pseudopotentials to the problem at hand is left to the end user, it is sometimes a non-trivial task to generate the data required. For instance, recent papers have come out trying to better produce pseudopotentials that agree with data from VASP based calculations. SIESTA supplies a database on its website of LDA (local density approximation) and GGA (generalized gradient approximation) pseudopotentials [43], but some of them are not properly configured for every type of simulation so taking the electron configurations and generating suitable potentials from the bundled ATOM code is needed [48] (as of version 4.1, the ATOM code is no long directly bundled with SIESTA; that version of the code is not used for the current work). Generating the pseudopotentials consists of telling the code how far the various electron orbitals extend in space and what the occupation of each valence orbital is. It is also

possible to perform simulations using all of the electrons (core and valence) but unnecessary for most cases because the core electrons do not interact. Frequently, generating a pseudopotential is needed to have empty atomic orbitals not included in the ones supplied by the database; generating a custom one or modifying other simulation parameters is needed.

The main issue with creating pseudopotentials in SIESTA is that there is not a standardized procedure for development. Recently, within the last 5 or so years, there has been a great deal of research on developing suitable pseudopotentials for the SIESTA code. These efforts have been designed to produce results as similar to other codes, most commonly VASP, as possible. This is especially true for heavier elements with many electrons and partially occupied d and f valence orbitals. In particular, the heavier cations in $LiNbO_3$ and $LiTaO_3$ require special attention since their orbital configurations are very important for predicting how the atoms interact with the surrounding system. It is less important for lighter elements that have been better studied (like Li, O, and Mg) which only have s and p valence orbitals.

2.2.4 *Ab initio* molecular dynamics

From both 2.1 and 2.3, it can be seen that in the 1980's, both computational methodologies began to mature– with DFT gaining new exchange and correlation approximations and classical MD gaining viable methods of performing new types of dynamics with new thermostats. Combining the two was not far away, especially due to the work by Car and Parrinello. Computational power has, however, lagged behind the theoretical frameworks. Only recently, with the dramatic increase in availability of super computing resources, have large scale simulations become possible.

Figure 2.1 has a force calculation step. Figure 2.2 can output forces. Combining those two elements together produces a very useful synergy where MD calculates the atom positions and motion and DFT provides the interatomic forces in what is known as *ab initio* molecular dynamics or AIMD. Many combination of codes can run AIMD simulations, but for the work presented here, SIESTA's built in algorithms for dynamic simulations are used. SIESTA provides a wide array

of ensembles for running calculations, but in order to make sure the simulations can be run in a reasonable time, the microcanonical ensemble is used (see table 2.2 for a partial list of ensembles; SIESTA is capable of running all of those listed)[43]. In the NVE (constant number of particles, constant volume, and constant energy) ensemble, the integrator used in computing the atom motion is also the simplest, the velocity Verlet algorithm.

There are two main types of AIMD– Born-Oppenheimer and Car-Parrinello[32]. Born-Oppenheimer based simulations use DFT to treat the forces and an MD algorithm of the user's choice to calculate motion. Car-Parrinello based simulations leverage electronic as well as physical degrees of freedom to perform calculations. Depending on the intended use case, either type of dynamics can be more taxing to calculate. For this work, it is crucial to consider how long the simulations take to complete.

Since AIMD used in the NVE ensemble only requires the use of DFT to produce the interatomic forces, it is also possible to write a separate code to act as the MD calculator and simply take the forces from the DFT calculations. An implementation of this is found in the ASE (Atomic Simulation Environment) python package [49]. The vast majority of the computational complexity in AIMD simulations is taken up by the DFT steps. Moving the atoms using the basic MD algorithm is far less computationally intensive.

When simulating E_d events, it is important to remove as many variables as possible and modify parameters to reduce simulation time. That is the reason why most of this work is performed with an initial system temperature of 0K. Random velocities can contribute to an increase in the energy required to displace an atom from its lattice site, which is a problem because more energy in the system results in a longer simulation time[50, 51, 52]. Also, if running any of the other types of ensembles for calculating atomic motion, thermostats must be considered. In a PKA threshold displacement simulation, the atomic motion of the PKA and displaced atoms should not interact with the thermostat because this would affect the results of both the resulting defect structures and energy required to displace an atom. Because of this, the NVE ensemble is the clear choice due to it not relying on the thermostat for computing atom motion in addition to its lower computational

20

cost. With increased availability of computational power, it becomes feasible to perform AIMD based calculations with more complex materials, like $LiNbO_3$ and $LiTaO_3$.

Chapter 3

MgO simulation

3.1 Introduction

Several ceramic oxides have been identified as candidates for use in waste forms for long term storage of transuranium elements or actinide transmutation targets due to their chemical and physical stability under irradiation conditions. Magnesium oxide, MgO, has been extensively studied for its applications in nuclear energy applications. MgO has been considered as an inert matrix for nuclear fuels, an insulator for fusion reactor designs, and for radioactive waste disposal. As a transmutation target, MgO is a promising candidate due its low neutron cross section and high thermal conductivity in addition to its radiation damage resistance. The rocksalt structure makes it ideal for studying basic effects of radiation damage and defect mobility in ceramic oxides. Previously figure 1.3 shows a rendering of the conventional MgO unit cell. The simple structure of MgO makes it one of the best materials to outline the various types of calculations required for DFT, MD, and AIMD analysis. MgO will be used to describe the basics of the processes involved in determining the static properties like the ground state of the material, the dynamic properties like threshold displacement energy, and the formation energies of defects in the material.

Before any dynamic simulations can begin, a thorough study of the ground state properties is necessary to validate the suitability of the simulation parameters and pseudopotentials. After the ground state properties are verified, the threshold displacement energies can be calculated through the method described in this section. Finally, the resulting defect structures and full displacement

pathways are described and analyzed. After defining the defect structures, the formation energies and energy required to create the defects can be calculated through a small number of static DFT calculations based on observed defect structures. As the material's composition increases in complexity, these types of studies become more difficult, as will be the case for $LiNbO_3$ and $LiTaO_3$ later.

3.2   Computational methods

AIMD simulations are performed using a modified version of the SIESTA code (version 2.0)[53]. Later calculations use newer versions (3.2, patch level 5) of the code since technical support and bug fixes are focused on the current version[43]. Future work will likely be done with the development version of the code (version 4.1); older versions lack developer support so it is important to keep that in mind when considering which version to use.
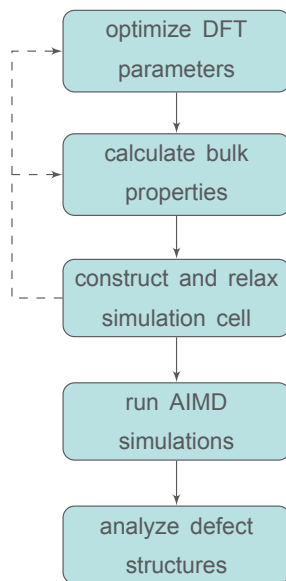
Figure 3.1: Flow chart illustrating the steps needed to configure an AIMD based E_d calculation. At any point in the flow chart, it may be required to go back and further optimize the simulation parameters.

Figure 3.1 shows the basic steps taken in configuring an AIMD simulation in SIESTA. The first step is to take an initial system configuration and find the ground state of the structure of interest.

Typically this requires utilizing the SIESTA pseudopotential database and researching lattice geometries. In this case, the pseudopotentials are selected from the SIESTA database[43]; both pseudopotentials are described by a norm-conserving Troullier-Martins type pseudopotential[54] factorized in the Kleinman-Bylander form[55]. The exchange correlation functional is determined within the GGA approximation as parameterized by Perdew, Burke, and Emzerhof (PBE)[56]. Ground states are chosen as $3s^2$ for Mg and $2s^2 2p^4$ for O.

Once the pseudopotential is properly configured, the next step is to fully relax the system to determine the ground state. This is done by using the experimentally determined lattice constants and allowing for the system to find a minimum energy through a conjugate-gradient (CG) minimization algorithm. Then, a simple static DFT calculation is performed on the relaxed structure along with modified DFT parameters (cutoff energy, K-point sampling in the Brillouin zone, and valance wave function configurations). A compromise between computational rigor and time taken for each calculation must be considered, hence the reason for selecting a cutoff energy of 70 Ry for the basis set and a K-point sampling of $1 \times 1 \times 1$ for the larger simulation cells and $8 \times 8 \times 8$ for initial relaxations.

3.2.1 Bulk material properties

Lattice constant and bulk modulus

Once the initial system configuration is selected and relaxed, bulk material properties can be calculated. The first set of calculations relating to the bulk properties is the determination of the lattice constant and bulk modulus by fitting to an equation of state. In this case, the Birch-Murnaghan equation of state[57] is used. The simpler Birch equation of state can also be used to fit these systems. The Murnaghan equation of sate 3.1 was first proposed by Murnaghan in 1944 [58]. It is a relationship between the pressure P, volume V, and bulk modulus K_0 of a material under compression.

$$P(V) = \frac{K_0}{K_0'} \left[\left(\frac{V}{V_0} \right)^{-K_0'} - 1 \right] \tag{3.1}$$

In connection to *ab intio* calculations, the equation of state can be integrated along with the relationship $P = \dfrac{-dE}{dV}$ to yield equation 3.2. This will be the primary form of the equation utilized because it is a direct relationship between volume, energy, and bulk modulus of a material.

$$E(V) = E_0 + K_0 V_0 \left[\frac{1}{K_0'(K_0' - 1)} \left(\frac{V}{V_0} \right)^{1 - K_0'} + \frac{1}{K_0'} \frac{V}{V_0} - \frac{1}{K_0' - 1} \right] \tag{3.2}$$

Later, the following equation of state was proposed by Birch and Murnaghan in 3.3 based on the work by Murnaghan as described above[57]. The Birch-Murnaghan equation of state was, like the equation developed by Murnaghan, based around cubic symmetry in crystals. This particular equation is the third-order isothermal equation of state for the strain components.

$$P(V) = \frac{3 B_0}{2} \left[\left(\frac{V_0}{V} \right)^{\frac{7}{3}} - \left(\frac{V_0}{V} \right)^{\frac{5}{3}} \right] \left\{ 1 + \frac{3}{4} (B_0' - 4) \left[\left(\frac{V_0}{V} \right)^{\frac{2}{3}} - 1 \right] \right\} \tag{3.3}$$

Applying the same procedure as before with the Murnaghan equation of state and integrating by pressure yields equation 3.4[57, 58].

$$E(V) = E_0 + \frac{9 V_0 B_0}{16} \left\{ \left[\left(\frac{V_0}{V} \right)^{\frac{2}{3}} - 1 \right]^3 B_0' + \left[\left(\frac{V_0}{V} \right)^{\frac{2}{3}} - 1 \right]^2 \left[6 - 4 \left(\frac{V_0}{V} \right)^{\frac{2}{3}} \right] \right\} \tag{3.4}$$

Taking the simulation cell volume from an initial relaxation, a range of volumes is selected around that value and the energy computed for each volume using a static calculation. The resulting energy-volume curve is then fitted to equation 3.4 using a Nelder-Mead optimization algorithm to find the best fit. With these optimized lattice constants and a value of the bulk modulus produced by the fitting algorithm, it is then possible to verify that the computational configuration selected produces reasonable simulations for comparison to other DFT and experimental work. The computation set up is then used to construct simulation super cells for performing the E_d simulations.

Elastic properties

For more complex structures, the results from fitting to equations of state are not reported. Fitting to an equation of state requires minimizing each free variable one at a time for the system in

question. For a cubic material, this requires varying only the lattice parameter, a. For more complex structures, this increases as N^2 for N number of free variables. It is easier to calculate the elastic properties of the material by deforming the material and determining the forces on the defected simulation cell. Calculating the elastic constants for a material requires taking a unit cell at ground state and applying a set of deformations and seeing the stress response. The process defined by the Materials Project begins with defining the deformations [59]

$$E = \frac{1}{2}\left(\boldsymbol{F}^T\boldsymbol{F} - \boldsymbol{I}\right) \tag{3.5}$$

Where $\boldsymbol{F}$ is the deformed matrix as defined by the set of:

$$\boldsymbol{F} = \begin{bmatrix} 1+\delta_1 & 0 & 0 \\ 0 & 1 & 0 \\ 0 & 0 & 1 \end{bmatrix}, \boldsymbol{F} = \begin{bmatrix} 1 & 0 & 0 \\ 0 & 1+\delta_1 & 0 \\ 0 & 0 & 1 \end{bmatrix}, \boldsymbol{F} = \begin{bmatrix} 1 & 0 & 0 \\ 0 & 1 & 0 \\ 0 & 0 & 1+\delta_1 \end{bmatrix} \tag{3.6}$$

$\delta_1 \in \{-0.01, -0.005, +0.005, +0.01\}$ is the set of strains selected for deformation; there are 12 calculations for normal strains. For shear strains, the set of deformation matrices in equation 3.7

$$\boldsymbol{F} = \begin{bmatrix} 1 & \delta_2 & 0 \\ 0 & 1 & 0 \\ 0 & 0 & 1 \end{bmatrix}, \boldsymbol{F} = \begin{bmatrix} 1 & 0 & \delta_2 \\ 0 & 1 & 0 \\ 0 & 0 & 1 \end{bmatrix}, \boldsymbol{F} = \begin{bmatrix} 1 & 0 & 0 \\ 0 & 1 & \delta_2 \\ 0 & 0 & 1 \end{bmatrix} \tag{3.7}$$

For shear modes, $\delta_2 \in \{-0.005, -0.0025, +0.0025, +0.005\}$ is used for the set of shear strains for a set of 12 calculations, leading to a total of 24 deformations applied to the system. After calculating the stress from the full set of 24 deformed cells, the software package pymatgen for the python programming language provided by the Materials Project provides an easy means for converting the stress response to elastic constants[60].

$$[\sigma] = [C][\epsilon] \, or \, \sigma_i = C_{ij}\epsilon_j \tag{3.8}$$

Equation 3.8 shows the generalized from of the relationship between stress σ and strain ϵ, using the stiffness tensor C. The stiffness tensor, in the generalized form is represented as

$$[c] = \begin{bmatrix} c_{1111} & c_{1122} & c_{1133} & c_{1144} & c_{1155} & c_{1166} \\ c_{2211} & c_{2222} & c_{2233} & c_{2244} & c_{2255} & c_{2266} \\ c_{3311} & c_{3322} & c_{3333} & c_{3344} & c_{3355} & c_{3366} \\ c_{4411} & c_{4422} & c_{4433} & c_{4444} & c_{4455} & c_{4466} \\ c_{5511} & c_{5522} & c_{5533} & c_{5544} & c_{5555} & c_{5566} \\ c_{6611} & c_{6622} & c_{6633} & c_{6644} & c_{6655} & c_{6666} \end{bmatrix} \equiv \begin{bmatrix} C_{11} & C_{12} & C_{13} & C_{14} & C_{15} & C_{16} \\ C_{12} & C_{22} & C_{23} & C_{24} & C_{25} & C_{26} \\ C_{13} & C_{23} & C_{33} & C_{34} & C_{35} & C_{36} \\ C_{14} & C_{24} & C_{34} & C_{44} & C_{45} & C_{46} \\ C_{15} & C_{25} & C_{35} & C_{45} & C_{55} & C_{56} \\ C_{16} & C_{26} & C_{36} & C_{46} & C_{56} & C_{66} \end{bmatrix} \tag{3.9}$$

Symmetry in the MgO unit cell means that there are really only three independent elastic constants, as shown in the stiffness tensor in 3.10, but for the sake of completeness and to ensure no computational error with the method above, all 24 deformations are performed.

$$[C] = \begin{bmatrix} C_{11} & C_{12} & C_{12} & 0 & 0 & 0 \\ C_{12} & C_{11} & C_{12} & 0 & 0 & 0 \\ C_{12} & C_{12} & C_{11} & 0 & 0 & 0 \\ 0 & 0 & 0 & C_{44} & 0 & 0 \\ 0 & 0 & 0 & 0 & C_{44} & 0 \\ 0 & 0 & 0 & 0 & 0 & C_{44} \end{bmatrix} \tag{3.10}$$

3.2.2 AIMD

An initial $3\times3\times3$ super cell of 216 atoms was used. Due to the use of periodic boundary conditions, however, it became necessary to increase the simulation cell size in several cases. Our previous work[50] has shown that increasing the cell size does not contribute significantly to the results of E_d calculations, so using a larger $4 \times 3 \times 3$ (288 atoms) and a still larger $4 \times 4 \times 3$ (384 atoms) proved necessary in certain cases. A time step of 1.0 fs was used for all simulations. A simple test to see if the time step is adequate is to perform two E_d calculations with different time steps to see if the results are the same. A time step of 1.0 fs compared nearly identically to a shorter time step of 0.5 fs for Mg[100] calculations so a 1.0 fs time step was determined to be reliable.
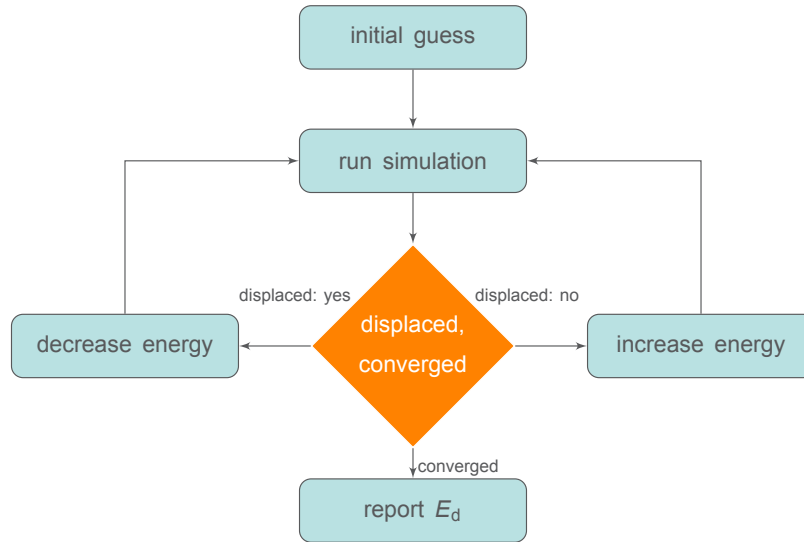
Figure 3.2: Method for determining threshold displacement energies.

To actually perform an E_d calculation, kinetic energy is supplied to an atom along a particular direction. In this case, three directions are chosen– [100], [110], and [111]. Figure 3.2 shows the basic method for determining the threshold displacement energy. An initial guess as to E_d is taken. A PKA in the relaxed simulation cell is then supplied with that energy. If it is displaced by the end of the simulation, then the energy is decreased and run again. Likewise, if it is not displaced, the energy is increased and the simulation run again. This process is repeated until results have converged within the specified tolerance. In this case, the tolerance was selected at 0.5 eV. Initial values for E_d are taken from the summary paper from Zinkle and Kinoshita[61] who suggest using 55 eV for codes like TRIM[10].

Usually the results are very obvious as to whether or not the PKA has been completely displaced, but the process needs human oversight to analyze the results. Figure 3.3 shows two traces of the x-y motion of the atoms in the case of the Mg[100] PKA that are 0.5 eV apart. Sometimes the time must be increased on the simulation because the PKA is still in motion by the end of the simulation. The defect structures can also then be reported. Care must be taken to ensure that the defects observed are stable within the context of the simulations. The longer the simulation progresses in time, the more energy is transferred to the atoms in the supercell. In a real material, there are many more atoms to transfer this energy to so it dissipates throughout the system. In small systems used

28
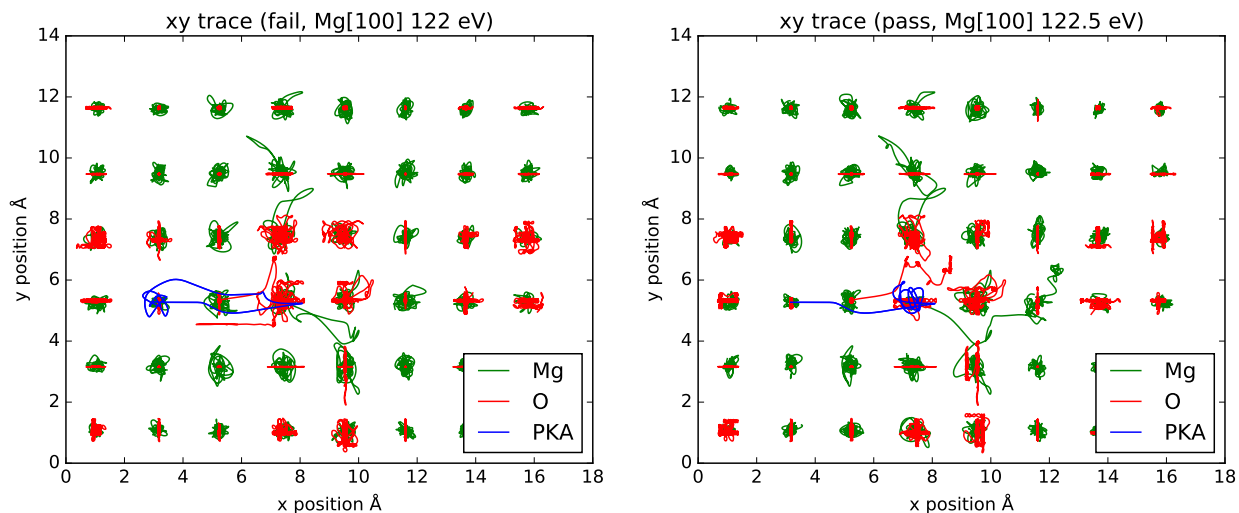
Figure 3.3: Traces of the x-y plane of a failure (left) and success (right) to produce a Frenkel pair. The difference in energy between the two is 0.5 eV.

in AIMD, this energy is kept within the system due to limitations on which types of thermostats can be used. If too much energy is transferred to the system, the result may not represent actual phenomena. If too much energy is allowed to dissipate to the rest of the atoms in the system, it a displacement chain can interact with itself requiring a larger simulation cell. The ideal situation would be to have the simulation progress long enough to produce a meta-stable defect structure within the bounds of the simulation parameters without going more than around 5 ps in time.

3.2.3 Defect chemistry

The next type of calculation required for this work involves the defect chemistry of point defects (vacancies and interstitials). Defect formation energy calculations requires calculating the energy of a pristine crystal, the defected crystal, and the compositional energy of the isolated atom.

$$E^F_{defect}(q) = E_T(defect, q) - E_T(pristine, q) + \mu_{defect} + q_{defect}E_F \qquad (3.11)$$

Equation 3.11 shows the defect formation energy for a single O vacancy in the structure with some charge q. The chemical potential of the defect is taken away from the pristine system, along with the associated energy due to the charge of the defect. For a simple system (like MgO), the chemical

potentials are relatively simple to catalog; they are the potential for Mg in Mg metal, O in O_2 gas, and the energies of Mg and O in MgO. Formation energies of isolated defects can also be calculated from utilizing ghost atoms in SIESTA.

3.3   Results

3.3.1   Lattice constant and bulk modulus
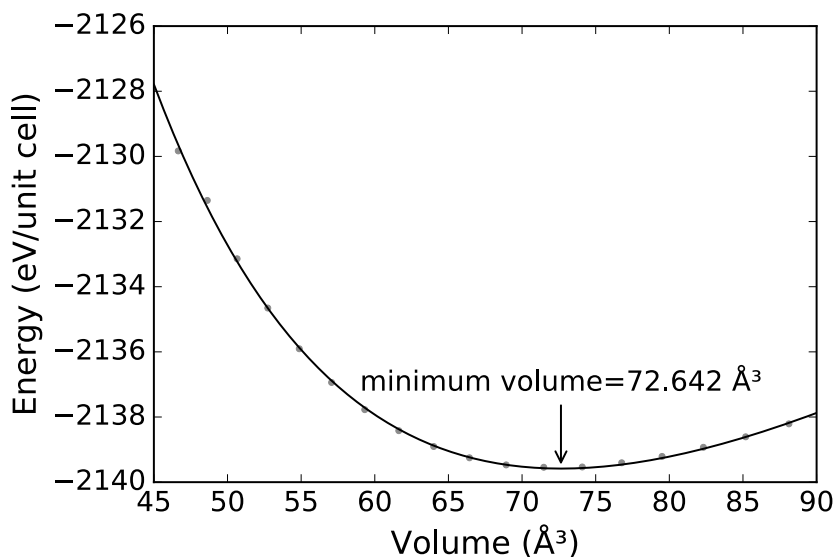
Figure 3.4: Energy versus volume of the conventional cubic MgO unit cell. The curve is fit to the Birch-Murnaghan equation of state. Minimum unit cell volume is also reported.

Figure 3.4 shows the variation in energy versus volume for the conventional cubic MgO unit cell. The fit to the data yields lattice parameter, a of 4.172 Å and a bulk modulus B 182 GPa at the minimum energy of the curve. The calculated value of a agrees well with experimental values ranging from 4.210 Å to 4.220 Å[62, 63, 64, 65, 66]. The bulk modulus is in fair agreement with experimental values of 163.9 [67], 162.20 [68], and 156 GPa[69]. It is also consistent with DFT based results of 172 [70], 185.9 [71], and 169.1 GPa [71].

3.3.2 Elastic constants

Performing the relaxations for the deformation set described in 3.10 using the lattice parameter of 4.172Å results in the following stiffness tensor (in GPa):

$$[C] = \begin{bmatrix} 302.64 & 113.03 & 113.51 & 0.33 & 0.23 & 0.14 \\ 113.58 & 302.06 & 113.51 & 0.07 & 0.60 & 0.70 \\ 113.58 & 113.03 & 302.55 & -0.64 & -0.19 & 0.13 \\ 0.11 & 0.56 & -0.69 & 177.29 & -0.42 & -0.70 \\ -0.59 & 0.10 & -0.69 & -0.37 & 177.25 & -0.51 \\ -0.59 & 0.56 & 0.07 & -0.12 & -0.14 & 177.62 \end{bmatrix} \qquad (3.12)$$

The symmetry of the structure means that the values for C_{11}, C_{22} and C_{33} should be equal. Within the tolerances set for determining elastic constants, this is indeed accurate. C_{12} values are within 0.55 GPa of each other which is well within acceptable tolerances. Values for C_{44} fall within a narrow range of 0.38 GPa, also within acceptable tolerances. The rest of the stiffnesses are to be reported as 0 since they are within the computational tolerances used in SIESTA. The final elastic constants are reported in table 3.1.

Table 3.1: Stiffnesses for MgO in units of GPa

C_{11}	C_{12}	C_{44}	source
302.42±0.25	113.37±0.24	177.39±0.17	this work
306.7	93.71	150.76	exp.[72]
297.08	95.36	156.13	exp.[73]
338	91	118	DFT[74]
286-352	91-108	158-188	LCAO[75]

3.3.3 Threshold displacement events

Results for E_d are summarized in table 3.2 and figure 3.6. After the atom is displaced from its lattice site, as either a replacement or interstitial, the simulations are further analyzed to determine whether or not the defect structure are stable at the end of the computational time limit. Sometimes, this requires increasing the simulation time and continuing the calculation further. Most of the defect

structures presented here stabilize at around 600 fs into the calculation. A further visual aid is figure 3.5 where the direction families are overlaid on a small MgO supercell.
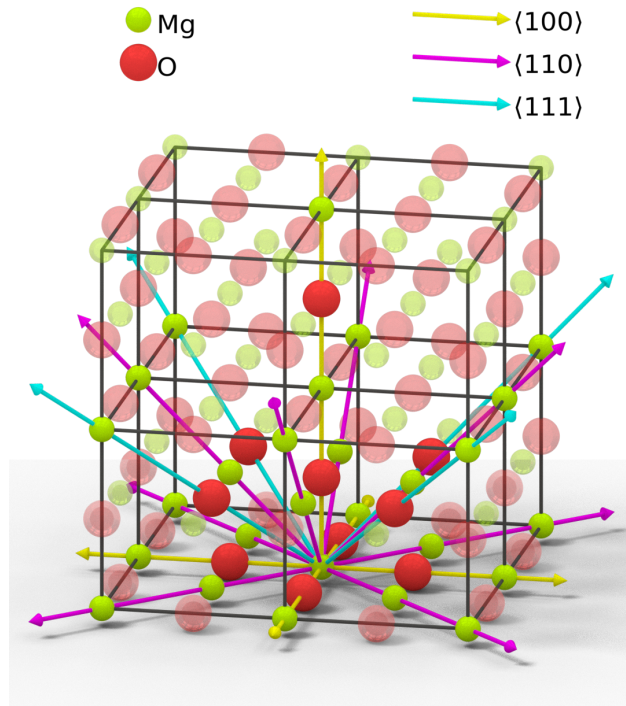
Figure 3.5: Directions tested overlaid onto a 2×2×2 MgO supercell

There are two main types of interactions for a lattice site during the simulation — either the original atom is replaced or a defect is formed at or near the site (such as interstitial formation). As detailed in the final defect state in table 3.2, a PKA produces at most two total interstitials that are stable at the end of the simulation. No simulation produces more than one Mg interstitial, and those that produce two interstitials (Mg [100], Mg [111], and O [100]) create either two O Frenkel pairs (O [100]) or one Mg and one O Frenkel pair. None of the O PKAs produce any stable O

replacements, but the Mg [111] recoil produces two.
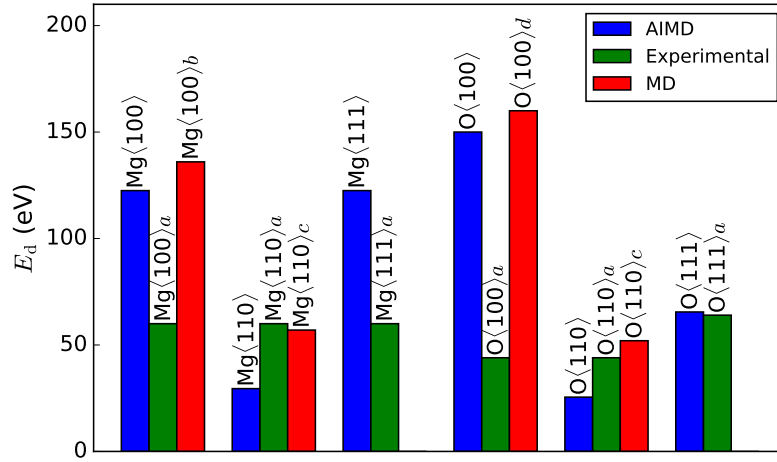
Figure 3.6: Comparison of E_d values calculated in MgO to several classical MD sources (b[4], c[5], and d[6]) and experimental (a[7]) data sets.

Table 3.2: E_d values for MgO pkas along with their final defect states

PKA	dir.	E_d (eV)	defect state
Mg	[100]	122.5	$Mg(PKA)_{Mg} + V_O + O_i + V_{Mg} + Mg_i$
Mg	[110]	29.5	$Mg(PKA)_{Mg} + Mg_{Mg} + V_{Mg} + Mg_i$
Mg	[111]	122.5	$Mg(PKA)_{Mg} + Mg_{Mg} + Mg_{Mg} + Mg_{Mg} +$ $O_O + O_O + V_O + V_{Mg} + O_i + Mg_i$
O	[100]	150.0	$V_O + V_O + O(PKA)_i + O_i$
O	[110]	25.5	$V_O + O(PKA)_i$
O	[111]	65.5	$V_O + O(PKA)_i$

During the Mg displacement event initiated along [100], the primary chain of displacements and replacements is along the initial [100] direction. The Mg PKA displaces the next atom (O) in the chain of atoms along [100]. That displaced O then forms an interstitial, leaving an O vacancy behind. Before finally coming to rest in a stable configuration, the displaced O atom displaces 3 Mg atoms along [011] immediately adjacent to it, but these three Mg settle back to their initial lattice sites eventually. The PKA then replaces the next atom (Mg) along the [100] direction and remains on that lattice site. The transferred energy is still high enough to push the next oxygen atom in the chain to displace the Mg atom adjacent to it along the [100] direction. The oxygen atom also causes some temporary displacements of Mg atoms in the [011] direction but those atoms return to their

original lattice sites at towards the end of the simulation. In total, two Frenkel pairs (1 Mg and 1 O) are formed and the PKA replaces the next Mg atom along [100].

Three Mg atoms in total are displaced during threshold displacement simulation for the Mg PKA along the [110] direction. The first two events along [110] are replacements. The PKA replaces the first neighboring Mg atom in the chain, which in turn replaces the second Mg atom in the chain. The third atom is then pushed into a cube-centered interstitial site where it remains stable until the end of the simulation.

The Mg [111] simulation involves the most displacement and replacement events of all the PKAs, and is therefore the most complicated to describe. The Mg PKA first collides with the closest O atom along [111], which is displaced. Temporarily, the Mg PKA resides on the vacant O site while additional vacancies are created that will eventually allow it to migrate. The O atom displaces an Mg atom and then rebounds along [00$\bar{1}$] where it forms a split interstitial (it eventually returns to its initial lattice site). The Mg atom that is displaced, still with momentum along [111], creates displacement chains of Mg and O parallel the [110] direction. The Mg chain along [110] produces two replacement events and terminates with the formation of an interstitial. Since the Mg atom that initiates the [110] oriented replacement chains leaves a vacancy, it provides a space for the PKA and adjacent atoms to migrate producing two more replacements. With the O site now vacated by the PKA, its original occupant returns by the end of the simulation. Finally, the [110] aligned O displacement chain produces 2 replacement events terminating in a split interstitial dumbbell along [110]. In total, six replacement events occurred (4 Mg and 2 O) and 2 Frenkel pairs are formed (1 Mg and 1 O).

The O [100] recoil, seen in creates 2 split interstitials: the first involving the PKA and the other involving an O displaced by the PKA. At first along the [100] direction, the PKA collides with the adjacent Mg atom. That atom gains enough kinetic energy to interact with the next O and to displace it, at a slight angle, toward the next Mg atom. Instead of displacing that Mg atom, the O recoil deflects slightly and passes through the next three (100) planes. After passing through those three atomic planes, the recoil forms a split interstitial. The PKA rebounds backwards along [100],

where it forms a split interstitial only half a unit cell behind its original lattice site.

The O [110] recoil has the lowest displacement energy and forms simplest defect configuration out of all studied cases. The PKA forms a split interstitial with the next O atom along [110]; there are no replacements or other interstitials that form.

Compared to the Mg [111] recoil event, the O [111] recoil produces a much simpler defect configurations. Along the [111] direction, the PKA displaces an Mg atom that in turn displaces another O atom. That Mg atom's trajectory turns to displace another Mg along [110], but both of these atoms eventually return to their original lattice sites. The displaced O also forms an unstable split interstitial and then returns to its original lattice site after around 400 fs. The PKA rebounded along [010] and forms a split interstitial which slowly travels over half a unit cell before coming to rest at the final interstitial site.

3.4   Discussion

3.4.1   AIMD defects

Once an atom has begun moving during the simulations, it generally maintains its path along the initial direction. Some of the recoils, like Mg[111], gradually change direction during the simulation, eventually aligning with a [110] direction. During all of the simulations, two primary interstitial defects evolved independently of the PKA species. As shown in figure 3.7, the Mg interstitial sits at a cube-centered site, with the cube being made of O and Mg. The O interstitial occupies a split interstitial configuration, shown in figure 3.8. The split O interstitials are suggested from theoretical calculations; DFT and classical molecular dynamics calculations have shown that these split O interstitials align along either a [110] or [111] direction, depending on the charge state of the defect. All of the O defects observed during these simulations, however, aligned with a [110] direction. Compared to DFT calculations, this configuration agrees with results produced by
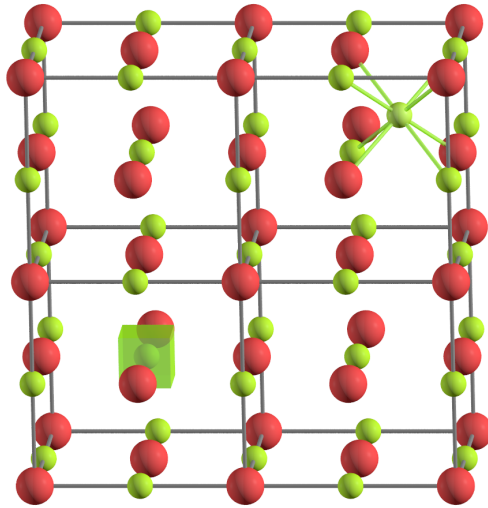
Figure 3.7: All Mg atoms are green; all O atoms are red. Observed Mg vacancy (cube) and interstitial (cube centered site) in all of the simulations.

neutrally charged O (O^0) interstitials[76, 77, 78].

AIMD show higher values for E_d for both Mg and O along [100] and [111] directions when compared to experimentally measured values[7]. This is to be expected due to the numerous sources of uncertainty such as electron beam misalignment and difficulties in the analysis of color centers; experimentally reported values are all close to $E_{d\ ave}$ of 55 eV regardless of the direction[61]. Additionally, the experimental results are reported at room temperature whereas these simulations are performed at low temperature (0 K) to ensure no influence of random velocities in the results. Along [110], AIMD gives a value about half that of the classical MD and experimental results. Previous studies using classical MD and AIMD have also shown that E_d obtained by AIMD is lower than that provided by classical MD[79, 80, 81]; partial-charge redistribution may be the contributing factor to the lower values for E_d .

3.4.2   Defect chemistry

For comparison to previously reported values, the defect formation energies and configurations need to be quantified and calculated. Based on initial testing and literature surveys, the minimal cell
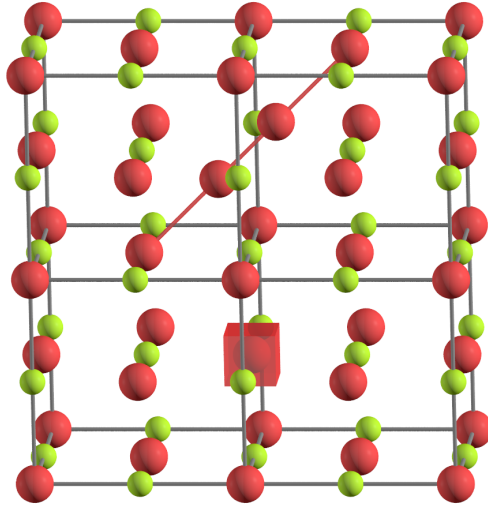
Figure 3.8: All Mg atoms are green; all O atoms are red. Observed O vacancy (cube) and interstitial (split [110] configuration) in all of the simulations.

size needed to report defects (interstitials and vacancies) in MgO is 216 atoms (which corresponds to a 3×3×3 supercell). This is also the minimum cell size required for performing E_d calculations. Larger cell sizes are not required since the values for formation energies of various point defects do not change.

The focus of this work is not to report defect formation energies so those are secondary to cataloging observed defects. Determining the types of defects produced during a collision cascade is necessary to understanding the processes by which a material is damaged under irradiation.

There are four equations used for calculating point defect formation energies:

$$E_{VO}^F(q) = E_T(M_{a-1}O_b, q) - E_T(M_aO_b, q) + \mu_{Mg} + qE_F \tag{3.13}$$

$$E_{VO}^F(q) = E_T(M_{a+1}O_b, q) - E_T(M_aO_b, q) - \mu_{Mg} + qE_F \tag{3.14}$$

$$E_{VO}^F(q) = E_T(M_aO_{b-1}, q) - E_T(M_aO_b, q) + \mu_O + qE_F \tag{3.15}$$

$$E_{VO}^F(q) = E_T(M_aO_{b+1}, q) - E_T(M_aO_b, q) - \mu_O + qE_F \tag{3.16}$$
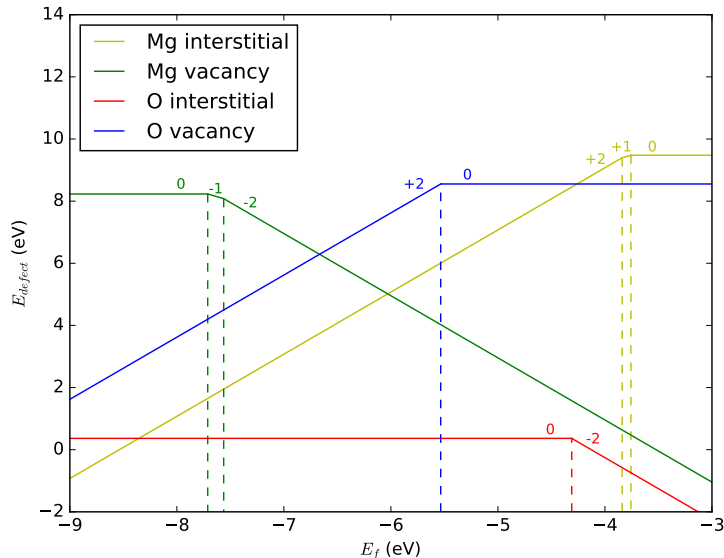
Figure 3.9: Defect formation energies for various defects in MgO

In each case, an atom is either added or removed from the system and the corresponding chemical potential is added or subtracted from the system. The Fermi energy, E_F, can be varied to show how the preferred charge state varies in the defected structures. Initial estimates use the Fermi energy calculated from a large (4×4×4 super cell) perfect crystal. Additionally, only the lowest energy state is considered for each of the charge states. The cross over points are marked with dashed lines. In general though, there is a prevalence of the neutral or doubly charged defect (Mg^{2+} and O^{2-}) states for all cases tested.

Care must be taken when considering charged Mg defects. Standard plane wave DFT methods poorly describe hole localization behavior for Mg vacancies and electron localization for Mg^{1+} interstitials. However, despite this short coming of standard plane wave DFT, the calculations have been performed anyway to serve as an example of the procedures involved with calculating defect formation energies. Additionally, there are some corrections that would need to be performed to limit the influence of finite size limits, but that is not the focus of the work presented here. Rather, the focus is on whether or not the trends in the defect formation energies are similar to those found in literature and an analysis of the defect structures present in the material. Defects produced from AIMD simulations might not be intuitive and tested using DFT methods.

For O defects (interstitials and vacancies) the preferred charge state, shown in figure 3.9, is either neutrally charged (O^0) or doubly charged (O^{2-}). This agrees with literature results and confirms that the singly charged defects are not energetically favorable in the material[76]. Neutrally charged Mg defects (Mg^0) are the only ones that are confirmed to be accurate due to the sort comings of DFT simulations with theses types of defects. Values for the other charge states are reported to demonstrate the technique, but they are not reliable.

3.4.3 Charge redistribution and orbital occupation
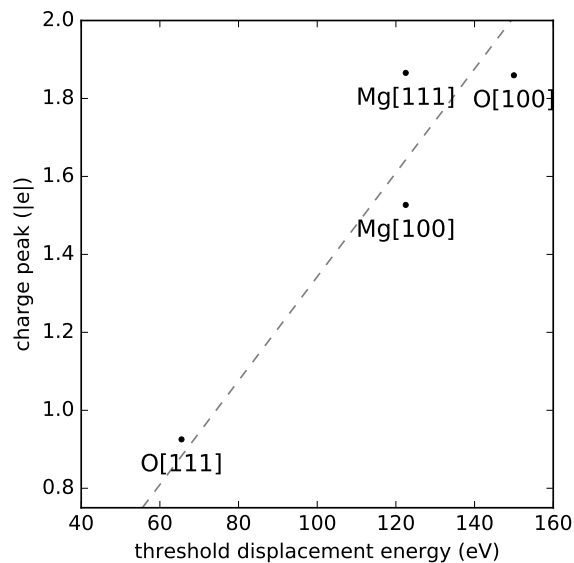
Figure 3.10: Partial charge transfer peak as a function of the threshold displacement energy for four of the PKAs, as annotated on the figure. The trend line is a linear fit to the data.

Thanks to the ability of AIMD based codes to provide information on the electronic structure changes during the course of a simulation, it is possible to figure out how the electrons of any atom in the simulation respond. One possible means of analysis is through monitoring the charge on the PKA as it travels through the lattice to determine how bonding changes. Other knock on atoms can be looked at as well to determine if their electronic structure changes significantly or if they form different types of bonds through the course of the simulation.

39

Another means of analysis using the electronic structures of the material is to monitor how the individual sublattices respond to the event. For instance, in MgO, it is possible to analyze the electron transfer or redistribution between the Mg and O sublattices. As the system nears its potential energy peak (where the atomic nuclei are closest to one another), there is an accompanying peak in the change in electron occupation of the sublattices. The peak in the charge redistribution is plotted in figure 3.10. They are measured by taking the total change in the effective Mulliken population of each sublattice over time. These peaks likely represent the maximum screened ion-ion interactions. This same trend has been observed in other AIMD simulations of low energy recoils as well[51].

3.5   Conclusion

Low energy recoil events in MgO are investigated using *ab initio* molecular dynamics simulations, based on density functional theory. The threshold displacement energies are shown to be highly direction dependent; displacements along single-species atomic chains occurred far more easily than those along mixed-species atomic chains. The two minimum E_d values (25.5 eV for O and 29.5 eV for Mg) both occur along the [110] single-species atomic chains. Low-energy recoil events of Mg and O form two types of interstitials; while Mg prefers to sit on cube centered sites, O prefers to form [110] aligned split interstitials. Compared to classical MD simulations, AIMD follows the same general trends. The lower values from AIMD calculations are attributed to partial-charge transfer assisted processes. Charge transfer potentials in classical MD may be a possible approach to better predict defect dynamics. Since MgO is used as a model material due to its simple electronic and atomic structure, these results are useful when considering the radiation effects in ceramic oxides and in particular the radiation resistance of crystals with the cubic crystal structure. The work on MgO helps to demonstrate computational techniques required for the analysis of more complex materials.

Chapter 4

Lithium niobate and lithium tantalate

4.1 Background

As mentioned in the introduction, $LiNbO_3$ and $LiTaO_3$ are important optical materials used widely in communication and other devices that rely on both of their elecro-optic, photorefractive, and non-linear optical properties. Recently, there has been interest in utilizing both materials in a mixture since their chemical and physical properties are so similar. To assist with preventing damage to these materials due to optical and other radiation concerns, they are often doped with MgO. They are often used in environments where intense optical radiation can damage the material, so understanding the processes by which damage occurs is essential to engineering more radiation resistant materials.

Both materials studied here share nearly the same atomic structure, as can be seen in the hexagonal cells in figure 4.1. The only difference between $LiNbO_3$ and $LiTaO_3$ at low temperatures is the larger cation– either Nb or Ta. Nb and Ta are in the same period on the periodic table so their valence electron structure are similar when surrounded by a coordinating O^{2-} octahedron, however their weights are considerably different with Ta weighting nearly twice as much as Nb. It is therefore expect that the collisions in the material with Nb atoms will transfer more momentum. Work done since the late 1980's has suggested that there are intrinsic defect complexes involving Nb or Ta antisite defects with compensating Li vacancies.
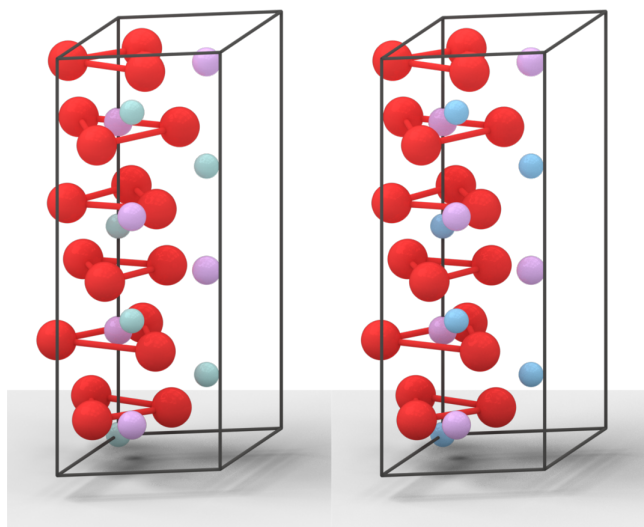
Figure 4.1: Hexagonal $LiNbO_3$ and $LiTaO_3$ unit cells. Bonds show O octohedra that surround Nb ions. Red atoms are O, purple atoms are Li, teal atoms are Nb, and blue atoms are Ta.

4.2 Methods

4.2.1 DFT parameters

All simulations in this work are performed with the SIESTA code version 3.2-pl5 [43]. Energy of the initial system needs to be minimized to ensure that the configuration will have no impact on the AIMD simulations later on. The specific parameters used for these simulations are chosen to ensure that the results are rigorous enough for precise results that allow simulations to be completed in a reasonable time scale due to the computational complexity of DFT and AIMD simulations.

Table 4.1: Pseudopotential configurations for all atoms used in $LiTaO_3$ and $LiNbO_3$ simulations.

species	orbital configuration	orbital cutoff radii (Bohr)
Li	$2s^1$	$r_s = 2.26, r_p = 2.26, r_d = 2.59, r_f = 2.59$
Nb	$5s^1 5p^0 4d^4$	$r_s = 2.85, r_p = 3.12, r_d = 2.52, r_f = 2.52$
Ta	$6s^2 6p^0 5d^3$	$r_s = 3.35, r_p = 3.66, r_d = 2.51, r_f = 2.42$
O	$2s^2 2p^4$	$r_s = 1.47, r_p = 1.47, r_d = 1.47, r_f = 1.47$

One of the main issues impeding wider adoption of the SIESTA code is the lack of suitable pseudopotentials. The lack of included and reliable Nb and Ta pseudopotentials resulted in having

to search for a well defined and properly tested pseudopotential. Work by Rivero et al focused on creating psuedopotentials for use in SIESTA that are intended to match VASP results as closely as possible[48]. The resulting pseudopotential configurations are shown in table 4.1. Two of the commonly available types for SIESTA calculations, LDA (local density approximation) and GGA (generalized gradient approximation) are intially considered. Due to only small differences in the predicted lattice energies and the long computational time for these particular material systems, LDA pseudopotentials are selected for the remainder of this work.

$LiNbO_3$ is a rhombohedral structure so the k-point mesh should be centered at (0.5, 0.5, 0.5) rather than the Γ point when considering defected structures[14]. Γ point calculations in rhombohedral structures can have difficulty converging, as demonstrated by work using the VASP code by Xu et al in ferroelectric $LiNbO_3$ [14] [18]. Smaller simulation cells, like those used for elastic constants, utilized a $5 \times 5 \times 5$ k-point mesh over the Brillouin zone generated by the Monkhost-Pack scheme. Simulation cells smaller than 120 atoms used a $2 \times 2 \times 2$ mesh and all other larger calculations used just the (0.5, 0.5, 0.5) point.

The benefit of using SIESTA compared with other codes is that it allows for DFT calculations involving ghost atoms[43]. Having ghost atoms in the system means it is relatively easy to calculate the chemical potential of each atom in the lattice. This is done by looking at the energy of a single atom in a lattice of ghost atoms. The results, which are the chemical potentials of the atoms in the system, are used in calculating defect formation energies. The formation energy of bulk $LiNbO_3$ and $LiTaO_3$ can be calculated by subtracting the chemical potentials of all constituent atoms from the bulk energy from the relaxed system. Having the chemical potential of one atom in the system allows for more reliable calculations of the defect structures as well. Defect structures are also calculated later on after determining the approximate geometry from AIMD.

4.2.2 Material properties

To ensure that the properties of the selected pseudopotential parameters are applicable to the given problem, several sets of calculations were done to calculate bulk elastic properties of the material. Bulk elastic properties provide a good measure of how the DFT parameters and pseudopotentials represent the interatomic forces in a system. Because we are intending to perform simulations that calculate forces based on DFT, the elastic properties give a reasonable metric to asses their suitability. There is no well defined method for developing SIESTA pseudopotentials so care must be taken to ensure that all selected parameters are going to produce viable results.

The basic procedure for calculating bulk properties is in two parts : first is using an equation of state to associate volume of the unit cell with energy of the unit cell; second is taking the unit cell with the minimum energy and subjecting it to a series of small strains to determine the interatomic forces acting upon the unit cell. If the properties predicted by these two tests match well with experimental and other DFT based results, work can proceed on calculating threshold displacement energies and defect states.

Lattice constant, lattice sites, and bulk modulus

For both $LiTaO_3$ and $LiNbO_3$ the same procedure for determining the optimal lattice configurations is used. Following the same procedure for MgO, the primitive system is relaxed with all parameters variable. Next, the volume of that optimal primitive cell is used to create a set of volumes $\pm10\%$ of the volume of the system. Since there are now two lattice constants, a and α, the rhombohedral angle, there need to be two sets of relaxations performed at each volume by varying α. At each volume, the minimum angle and corresponding lattice parameter are determined and then the minimum energy of each of those curves can be used to fit to 3.4. This yields a minimum volume for the system as well as a bulk modulus. The value for α for the minimum volume can also be calculated which yields the minimum lattice parameter a.

Elastic properties

The same procedures used for MgO are used here. The optimum lattice parameters are used to create a conventional (hexagonal) unit cell for $LiTaO_3$ and $LiNbO_3$. The conventional cell is then subjected to the same series of 24 deformations recommended by the materials project and analyzed to produce the elastic constants[59]. The same values for δ in the deformation set for MgO are used for $LiNbO_3$ and $LiTaO_3$.

$$[C] = \begin{bmatrix} c_{11} & c_{12} & c_{13} & c_{14} & 0 & 0 \\ c_{12} & c_{11} & c_{13} & -c_{14} & 0 & 0 \\ c_{13} & c_{13} & c_{33} & 0 & 0 & 0 \\ c_{14} & -c_{14} & 0 & c_{44} & 0 & 0 \\ 0 & 0 & 0 & 0 & c_{44} & c_{14} \\ 0 & 0 & 0 & 0 & c_{14} & c_{66} \end{bmatrix} \tag{4.1}$$

Equation 4.1 shows the matrix of stiffnesses for rhombohedral crystals from equation 3.9. The elastic constants presented in table 4.3 do not include c_{66} because it is not an independent elastic constant; it is a function of c_{44} and c_{14}.

4.2.3 AIMD

Once suitable bulk properties are calculated and the validity of the DFT parameters confirmed, further testing involving the threshold displacement events can commence. First, a sampling of directions along nearest neighbor directions is selected. The nearest neighbor directions are chosen because of the limitations of the simulations. The higher the index of the direction, the longer the PKA will travel in the system before striking another atom. Selecting the nearest neighbors ensures that an atomic collision can occur and the displacement event will not interact with itself due to periodic boundary conditions. This becomes more of a concern as PKA energy increases.

To ensure an appropriate number of atoms is used for the simulation, quick calculations are performed to determine the system energy convergence with simulation cell size. In a defect free

system using the same DFT parameters as the threshold displacement event, the energy is found to converge at system sizes somewhere between 120 and 240 atoms. This does not mean that the defect formation energies converge at these values but rather, that there is a minimum system size to ensure the minimization of the size effect on the threshold displacement event initially.

To begin the PKA displacement simulation, the relaxed test system is initialized for several hundred MD steps to ensure that the system has had time to equilibrate. For different numbers of atoms this can take longer or shorter. Rather, it is run till the average velocity of all similar atoms is the same. Once the system is initialized, kinetic energy is supplied to the PKA along the specified direction. The system is monitored to see if the supplied energy is sufficient to form a defect. If the supplied energy displaces an atom, then another simulation is run with a lower energy to within a tolerance of 1 eV. The same procedure is repeated if an atom is not displaced except the energy is increased instead. The system can be let run longer or shorter depending on the desired properties. For most cases in $LiNbO_3$, the defect will be produced within the first 200 fs. If the threshold displacement energy is finally determined, care is taken to ensure that the defect is stable within a feasible time scale. Usually this requires a supplementary calculation at a longer time scale of up to a maximum of 2 ps. Longer time scales are, however, problematic because the chain of recoils produced may have more of a chance to interact with itself due to periodic boundary conditions.

Additionally, to conserve computational time, all calculations are performed at an initial temperature of 0K and with the NVE ensemble. This ensures that there is no influence of random velocities and that the system is indeed at its ground state when AIMD calculations begin. The higher the temperature, the higher the computational cost. Already these are costly to calculate due to the number of simulations required per threshold displacement event. The NVE ensemble is chosen because if there is a thermostat in the system, the cell size must be large enough that the PKA and subsequent recoil events do not interact with the thermostat. This can cause the simulation cells to become very large in some cases, which is a consideration for this work due to the already computationally intensive task of running DFT calculations on larger simulation cells.
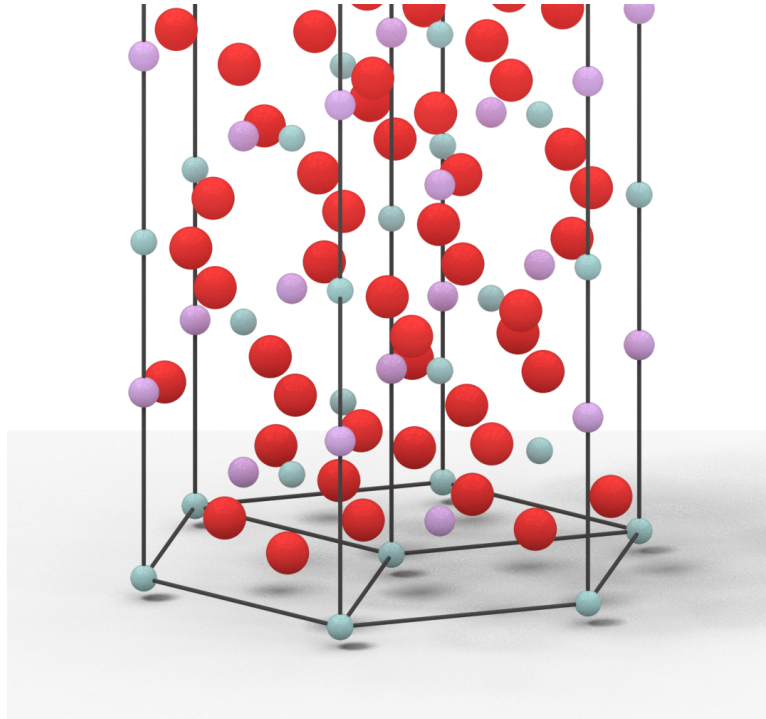
Figure 4.2: A hexagonal $LiNbO_3$ unit cell with all atoms shown. Red atoms are O, teal atoms are Nb, and purple atoms are Li

Directions for threshold displacement simulations are first chosen as either in the basal plane or normal to the basal plane of the hexagonal unit cell. Then additional directions are chosen based on nearest neighbor atoms and which directions are likely to produce collisions within the simulation cell. The hexagonal unit cell is shown in figure 4.2 and the chosen directions are overlaid in figure 4.3 on a half unit cell.

4.2.4 Defect chemistry

The final threshold displacement simulation produces a defect structure. These defects are sometimes unintuitive so it is useful to characterize these structures. Additionally, there has been no work characterizing defects in $LiNbO_3$ or $LiTaO_3$ utilizing an LCAO based code like SIESTA. All of the analysis so far has utilized plane-wave DFT or empirical calculations partially based on experimental observation. Since the structure is non-cubic, charged defects are increasingly
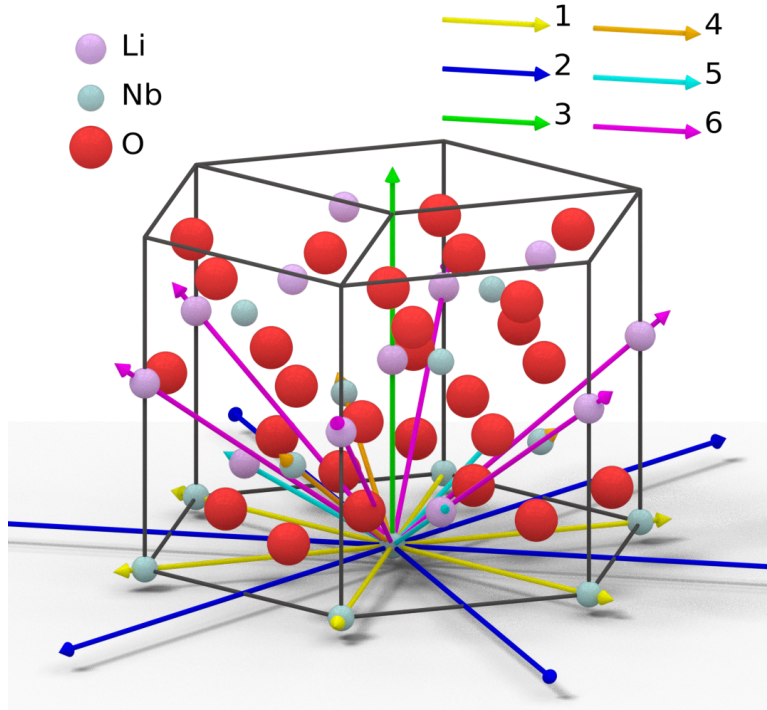
Figure 4.3: Directions used for threshold displacement simulations overlaid onto half of a hexagonal unit cell along the c axis. Directions 1 and 2 are in the basal plane of the unit cell. Direction 3 is normal to the basal plane. Directions 4, 5, and 6 are chosen as nearest neighbor directions for cations or cations.

difficult to calculate, due to the affects of the periodic boundary conditions. Therefore testing is done to ensure that the size of cell used (at minimum 270 atoms) for defect and E_{d} calculations is adequate to eliminate size effects. Beyond 360 atoms, the simulations become too computationally intensive to perform within any sort of reasonable time limit. Additionally, a more lenient force tolerance of $0.01 eV/$Å is required for the structures to converge at all. The higher force tolerances used on elastic constant calculations are too constraining for calculations to converge.

4.3 Results

4.3.1 Lattice constant and bulk modulus

The first set of relaxations for LiNbO$_3$ and LiTaO$_3$ is to determine the optimal lattice parameters based on the chose pseudopotentials. This requires an initial general relaxation of the system to form a guess for the lattice parameters. Since there are two degrees of freedom in the rhombohedral lattice parameters, $a_{hexagonal}$ and $c_{hexagonal}$ for the hexagonal system or $a_{rhombohedral}$ and $\alpha_{rhombohedral}$ for the rhombohedral system, both parameters need to be probed as shown below.

LiNbO$_3$

(a)   (b)
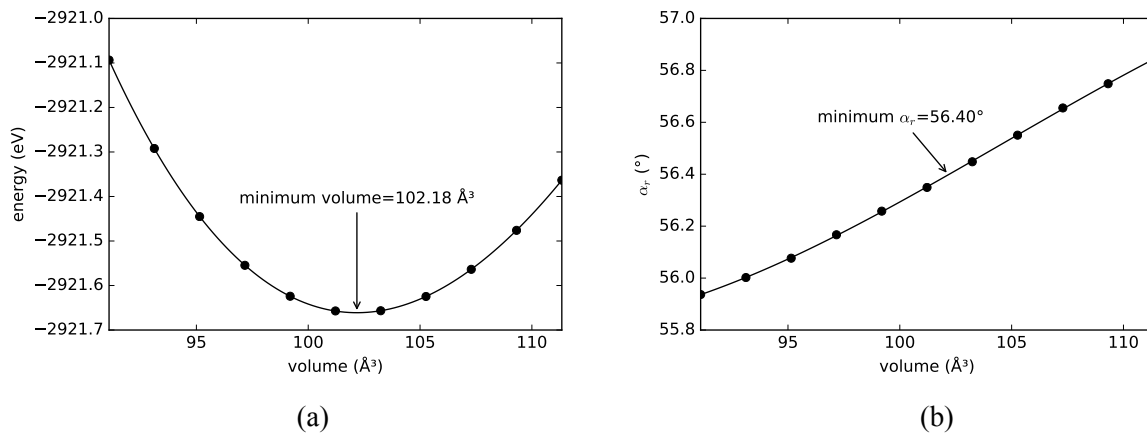
Figure 4.4: The fit to the equation of state for LiNbO$_3$. 4.4a shows the fit to the minimum energy at each of the selected volumes to the Birch-Murnaghan equation of state. The corresponding minimum volume is labeled. 4.4b shows the minimum value for α in each volume set from 4.4a

Plotted in figure 4.4a is the minimum energy for each volume selected. Each one of these minima plotted corresponds to an accompanying value for α in the rhombohedral system. The values for α are shown in figure 4.4b. Using simple linear interpolation, the minimum volume corresponds to a minimum value for α which is shown on the figure. Since two of the constraints are know, it is trivial to calculate the remaining lattice parameter.

Table 4.2 shows the results of the derived lattice constants compared to values available in the literature. The results presented here are consistent with both experimental and DFT based

49

Table 4.2: Lattice constants derived form the equation of state fit in figure 4.4a

reference	a_{hex}(Å)	c_{hex}(Å)
-	5.11	13.58
[82](experiment)	5.15	13.9
[83](DFT)	5.15	13.8

calculations (within 1% of reported values)[82, 84, 83, 14, 18].

LiTaO₃
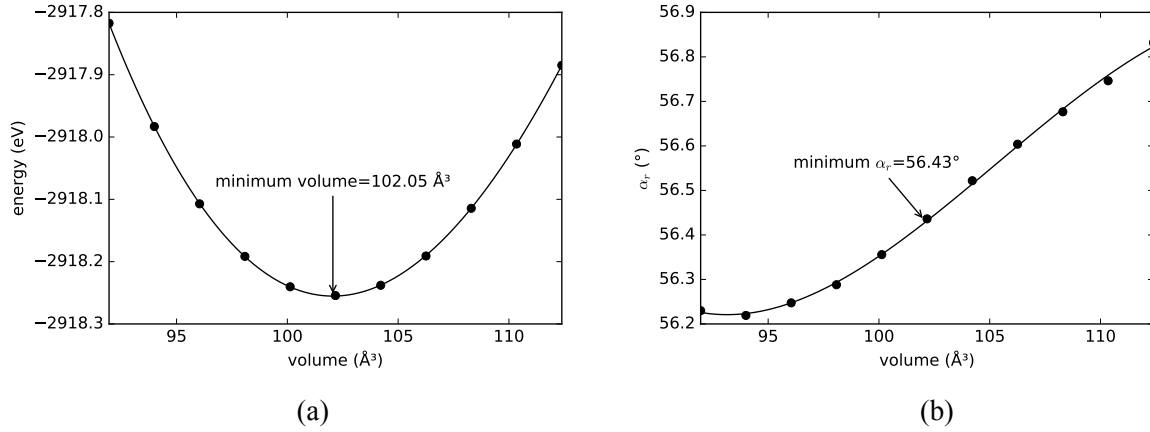
Figure 4.5: The fit to the equation of state for LiTaO₃ . 4.4a shows the fit to the minimum enery at each of the selected volumes to the Birch-Murnaghan equation of state. The corresponding minimum volume is labeled. 4.5b shows the minimum value for α in each volume set from 4.5a

The lattice constants reported here for LiTaO₃ are within 1% of reported experimental and DFT based results[82, 83]. The reported lattice parameters for LiTaO₃ , it should be noted, are very similar to those reported for LiNbO₃ ; this is expected and discussed previously, but the lattice parameters should be very similar especially at ground state and low temperature. As a first estimate of the material properties, the lattice constants and volume confirm that the ground state properties are consistent with known experimental values.

4.3.2 Elastic constants

Since this work is utilizing newly parameterized pseudopotentials, the forces between atoms need to be verified to ensure that further simulations are valid. Most work performed on $LiNbO_3$ and $LiTaO_3$ with respect to their elastic properties do not test the full set of deformation matrices and use arguments of symmetry to reduce the number of simulations required. The full set is used here for completeness. It should also be noted that c_{66} is not an independent elastic constant (it is a function of c_{14} and c_{44}) in the rhombohedral structure so it is not reported.

$LiNbO_3$

Table 4.3: Elastic constants for $LiNbO_3$. Units of $10^{10} \ N \cdot m^{-2}$

Ref.	c_{11}	c_{12}	c_{13}	c_{14}	c_{33}	c_{44}
this work	24.1	9.2	7.8	0.9	23.2	7.6
experiment [85]	19.8	5.5	6.5	0.79	22.8	6.0
empirical [86]	21.30	8.91	6.90	-3.67	22.28	6.92
DFT [83]	19.69	5.48	6.64	0	22.54	5.88

The DFT results form this work match reasonably well to previously calculated values, as shown in table 4.3. The values that do not match closely, namely c_{11} and c_{12}, are likely due to the stricter tolerances used in this calculation than in the literature. Especially for DFT and other computational results, there is a lack of information about explicit calculation parameters (the deformation matrices and force tolerances). Even the material project pymatgen python package gives a warning when fitting data from VASP and other DFT calculations to carefully consider the curve being fit[59]. If the deformation is too great, then the fit is poor.

$LiTaO_3$

The results in table 4.4 match more closely with experimental and other DFT results than those presented from $LiNbO_3$ in table 4.3. The results from $LiNbO_3$ and $LiTaO_3$ in this work are very

Table 4.4: Elastic constants for $LiTaO_3$. Units of $10^{10}\ N \cdot m^{-2}$

Ref.	c_{11}	c_{12}	c_{13}	c_{14}	c_{33}	c_{44}
this work	25.9	8.2	8.1	-0.4	25.2	10.0
experiment	23.3	4.7	8.0	-1.1	27.5	9.4
DFT(PW-GGA)	23.52	6.38	8.77	0	26.41	10.21

similar that the discrepancy is reliant on the Nb atom (the only major difference between the two structures) as the source of error. Otherwise, if c_{11} is ignored, the results are consistent.

4.3.3 Threshold displacement simulations

LiNbO$_3$

Table 4.5: Threshold displacement energies from AIMD calculations along various crystallographic directions described in figure 4.3 for $LiNbO_3$.

PKA	direction	$E_{\rm d}$ (eV)	defect structure
Li	1	14	$V_{Li(PKA)} + Li(PKA)_i$
Li	2	22	$V_{Li(PKA)} + Li(PKA)_i$
Li	3	67	$V_{Li(PKA)} + Li(PKA)_i + V_{Li} + Li_i + V_{Nb} + Nb_i$
Li	4	29	$V_{Li(PKA)} + Li(PKA)_i$
Li	5	29	$V_{Li(PKA)} + Li(PKA)_i$
Li	6	36	$V_{Li(PKA)} + Li(PKA)_i$
Nb	1	32	$V_{Nb(PKA)} + Nb(PKA)_i$
Nb	2	26	$V_{Nb(PKA)} + Nb(PKA)_i + 2V_{Li} + 2Li_i$
Nb	3	35	$V_{Nb(PKA)} + Nb(PKA)_i + V_{Nb} + Nb_i + V_{Li} + Li_i$
Nb	4	48	$V_{Nb(PKA)} + Nb(PKA)_i + V_{Nb} + Nb_i + V_O + O_i$
Nb	5	43	$V_{Nb(PKA)} + Nb(PKA)_i + 2V_O + 2O_i$
Nb	6	26	$V_{Nb(PKA)} + Nb(PKA)_i + V_{Li} + Li_i$
O	1	23	$V_{O(PKA)} + O(PKA)_i + V_O + O_i$
O	2	24	$V_{O(PKA)} + O(PKA)_i + V_O + O_i$
O	3	21	$V_{O(PKA)} + O(PKA)_i + V_O + O_i$
O	4	30	$V_{O(PKA)} + O(PKA)_O + O_O + O_i$
O	5	18	$V_{O(PKA)} + O(PKA)_O + O_i$
O	6	20	$V_{O(PKA)} + O(PKA)_i + V_O + O_i + 2V_{Li} + 2Li_i$

Displacements along directions 4 and 5 for Nb PKAs required longer simulations, up to 1.5 ps but produced similar defect structures compared to the other directions tested. The highest threshold displacement energies observed are along the [001] for Li. Likely, this is because it immediately

encounters a Nb atom as the nearest neighbor before rebounding to a high symmetry site in the opposite direction of the initial PKA momentum. Li also proved easiest to displace (directions 1 and 2, corresponding to recoils in the basal plane) Nb PKAs on the other hand are much more likely to have similar threshold displacement energies (ranging from 26 to 48 eV).

LiTaO$_3$

Table 4.6: Threshold displacement energies from AIMD calculations along various crystallographic directions described in figure 4.3 for LiTaO$_3$.

PKA	direction	E_d (eV)	defect structure
Li	1	6	$V_{Li(PKA)} + Li(PKA)_i$
Li	2	18	$V_{Li(PKA)} + Li(PKA)_i$
Li	3	30	$V_{Li(PKA)} + Li(PKA)_i + V_O + V_{Ta} + O_i + Ta_i$
Li	4	13	$V_{Li(PKA)} + Li(PKA)_i$
Li	5	15	$V_{Li(PKA)} + Li(PKA)_i$
Li	6	30	$V_{Li(PKA)} + Li(PKA)_i$
Ta	1	17	$V_{Ta(PKA)} + Ta(PKA)_i + V_{Li} + Li_i$
Ta	2	21	$V_{Ta(PKA)} + Ta(PKA)_i + 2V_{Li} + 2_{VO} + 2Li_i + 2O_i$
Ta	3	29	$V_{Ta(PKA)} + Ta(PKA)_i + V_{Ta} + Ta_i + 2V_{Li} + 2Li_i$
Ta	4	28	$V_{Ta(PKA)} + Ta(PKA)_i + 2V_{Li} + 2Li_i$
Ta	5	23	$V_{Ta(PKA)} + Ta(PKA)_i$
Ta	6	28	$V_{Ta(PKA)} + Ta(PKA)_i + 2V_{Li} + 2Li_i$
O	1	29	$V_{O(PKA)} + O(PKA)_O + V_O + O_i$
O	2	22	$V_{O(PKA)} + O(PKA)_i$
O	3	18	$V_{O(PKA)} + O(PKA)_i$
O	4	60	$V_{O(PKA)} + O(PKA)_i + V_{Ta} + Ta_i + V_{Li} + Li_i$
O	5	16	$V_{O(PKA)} + O(PKA)_i$
O	6	50	$V_{O(PKA)} + O(PKA)_O + V_O + O_i$

Table 4.6 shows the measured threshold displacement energy along with the associated defects in the material for PKAs in LiTaO$_3$. For most of the lighter ions, Li and O, the final defect state is quickly reached. Li has lower overall E_d values in LiTaO$_3$ compared with LiNbO$_3$, as demonstrated by the fact that O is the most difficult ion to displace in LiTaO$_3$, with an energy lower than that required for producing the highest energy defect in LiNbO$_3$ (Li along [100]).

The data presented in tables 4.5 and 4.6 show similar trends for E_d values in both materials. One value of 120 eV as the threshold displacement energy experimentally determined by Hodgson [15] is nearly twice as large as the highest observed value (the 67 eV E_d from the Li [001] PKA in

$LiNbO_3$).

4.4 Discussion

4.4.1 Weighted average E_d

If, based on figure 4.3, we weight the resulting threshold displacement energies according to the total number of similar directions in the structure, we end up with the results in table 4.7.

Table 4.7: Weighted averages for E_d calculations

PKA	E_d (eV)	source
	$LiNbO_3$	
Li	29.74	this work
Nb	33.58	this work
O	22.42	this work
Li	25	TRIM[22]
Nb	25	TRIM[22]
O	28	TRIM[22]
	$LiTaO_3$	
Li	19.26	this work
Ta	24.42	this work
O	36.79	this work

Average threshold displacement energy values provided in table 4.7 agree well with the values used for TRIM calculations in previously published work on $LiNbO_3$ [22]; if the results are too dissimilar, the calculations from TRIM would not match experimental results well. In general, based on the information in table 4.7, the trend is that cations (Li and Ta) are easier to displace in $LiTaO_3$ than cations (Li and Nb) in $LiTaO_3$. Anions (O) in both structures follow the opposite trend, where it is easier to displace an O in $LiNbO_3$ than it is in $LiTaO_3$. Since the defect behavior of O interstitials is more complicated than that of any cations, further inquiry into the exact nature of these interstitials may be necessary,discussed later. O interstitials are not energetically favorable so are unlikely to be measured and detected.

4.4.2 AIMD defects

As detailed in tables 4.5 and 4.6, there are a number of defects produced in each AIMD simulation– a Frenkel pair is always formed along with auxiliary defects, usually in the form of additional Frenkel pairs. Figures 4.10 and 4.6b shows a bar graph of the information in tables 4.5 and 4.6 respectively.
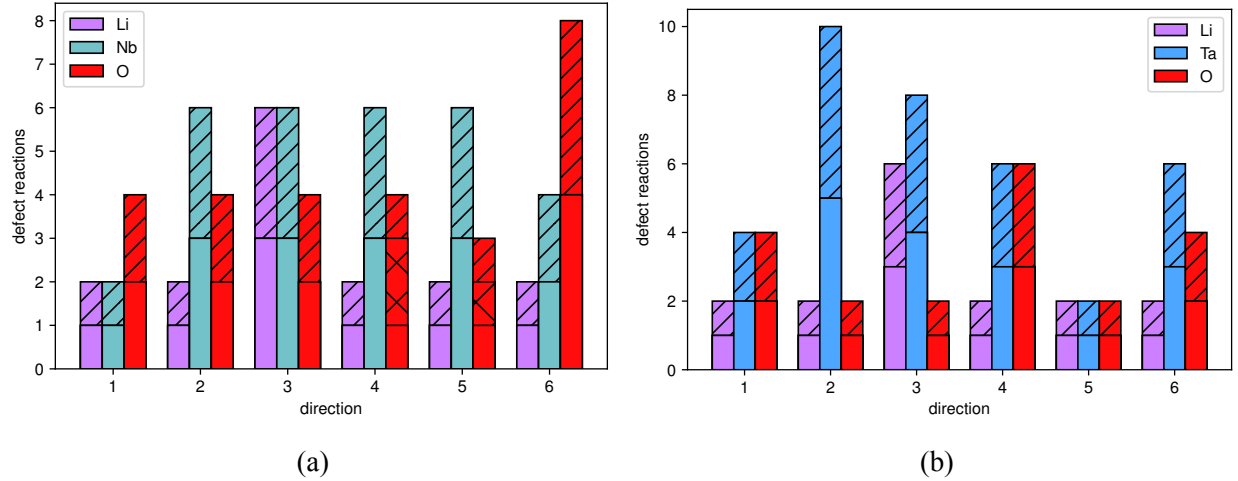
Figure 4.6: Total number of defect reactions for each threshold displacement simulation. Solid regions are interstitials, single hatched regions represent vacancies, and double hatched regions are replacements. Figures 4.6a and 4.6b use different scales.

Overall, there are three types of defect interactions in the E_d events: PKA Frenkel pair formation, replacement, and auxiliary Frenkel pair formation. Most displacement events produced either one or two Frenkel pairs. The only replacements involve O in $LiNbO_3$ along directions 4 and 5. Compared to the cations in their respective structures, O forms relatively few defects beyond the initial Frenkel pair. In some cases there are additional defects like replacements in the case of directions 4 and 5 for $LiNbO_3$ or additional cation defects in the cases of direction 6 in $LiNbO_3$ and direction 4 in $LiTaO_3$. Otherwise, there are only O Frenkel pairs (on average one per E_d event in $LiTaO_3$ and two per E_d event in $LiNbO_3$).

Figure 4.7: Location of the observed defects along the c axis as shown by the black atom overlaid on the hexagonal unit cell (right) and the split O interstitial shown overlaid on the hexagonal unit cell(left)

4.4.3 Defect configurations

Cations

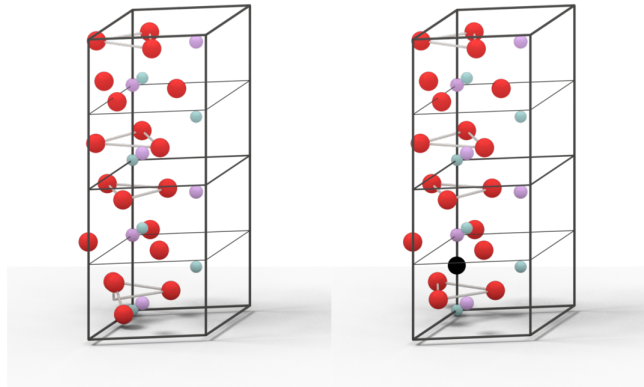The primary feature of the heavy cation displacements (Nb or Ta), is the response in the Li sublattice to the cation interstitial. There is a slight displacement of all surrounding Li ions to compensate for the larger interstitial. This displacement occurs along the direction normal to the basal plane. The site is marked in figure 4.7The largest amount of free space is along these planes so the displacement in this manner makes sense– the Li ions move closer to the high symmetry site rather than into the site. Oxygen atoms stay on their lattice sites for the most part in these simulations. Oxygen atoms are more strongly attached to the larger cation species due to the larger charge difference. For comparison between $LiNbO_3$ and $LiTaO_3$, the Li interstitial resides at 2.20Å along the c axis whereas the Nb and Ta interstitials reside slightly lower at 2.03Å.

There are no replacement interactions observed for any cation displacement event. As shown in prior DFT work, there needs to be compensating Li vacancies for an Nb or Ta defect to occupy an Li site. Since there are no compensating Li compositional vacancies present in the structure, there are no replacement events. The large volume of interstitial sites facilitates this process as it is

56

more energetically favorable to come to rest at an interstitial site than at a higher energy displaced defect site.

Whenever there is a large energy supplied to the system along the c-axis, there is a corresponding displacement and return of a large amount of Li in the system. They will move towards the high symmetry interstitial site and then back to their original lattice site.

Anions
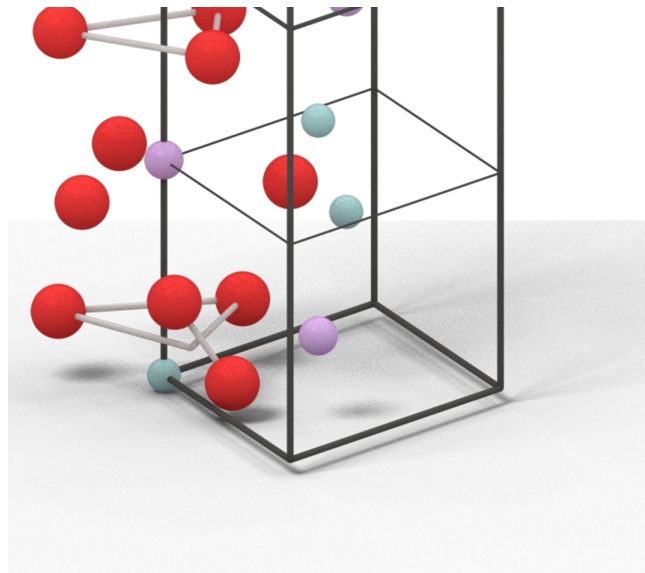
Figure 4.8: Close up and rotated version of the split oxygen interstitial in figure 4.7

Anion displacements are more complicated than cation displacements due to the larger number of possible defect sites. The structure displayed in figure 4.8 shows the close up version of one of the configurations for O interstitials in $LiNbO_3$ and $LiTaO_3$. In $LiNbO_3$ and $LiTaO_3$ it forms an angle with the c axis of 33.5° . The pair is not centered on the original lattice site, being offset slightly. There are therefore six total configurations for this defect– one at each lattice site, and one for each offset, left or right, which changes the offset angle to -33.5°. The exact positions of the atoms comprising the split interstitial in $LiNbO_3$ are $x_1 = 1.24$Å, $y_1 = -0.33$Å, and $z_1 = 1.50$Å for the first O and $x_2 = 1.92$Å, $y_2 = 0.35$Å, and $z_1 = 0.33$Å for the second O. If there is enough energy in the system, there may be some oscillation of the spacing between the split interstitial so

the exact bond length is subject to change during the simulation. The atom positions reported for the O interstitials are after relaxation to ensure that this vibration is not present.

4.4.4 Defect chemistry

Table 4.8: Total energy for each compound (per formula unit) near and at the stoichiometric composition on the phase diagram for $LiTaO_3$ and $LiNbO_3$

Compound	energy (eV)
O_2 gas	-430.76
Li metal (FCC)	-7.7095
Nb metal (FCC)	-143.00
Ta metal (FCC)	-142.35
Li_2O	-452.38
Nb_2O_5	-2464.6
NbO_2	-1014.0
TaO	-572.84
Ta_2O_5	-2451.9
$LiNbO_3$	-1459.7
$LiTaO_3$	-1455.0

The first step in calculating defect chemistry for the various materials analyzed is to determine the reference states for each chemical compound that is close in composition to either $LiNbO_3$ or $LiTaO_3$. Then the energy per formula unit of each of these compounds is calculated for their ground state configure (reported in table 4.8). These ground state energies per formula unit are then used to calculate the energy per atom for each specie at the various points on their respective phase diagrams.

LiNbO$_3$

Taking the chemical potentials from table 4.8, the formation energies of various defects along points A-F in figure 4.9 can be calculated. The main reason for selecting these points in the phase diagram is for easy comparison to literature and to verify the formation energies at conditions similar to the
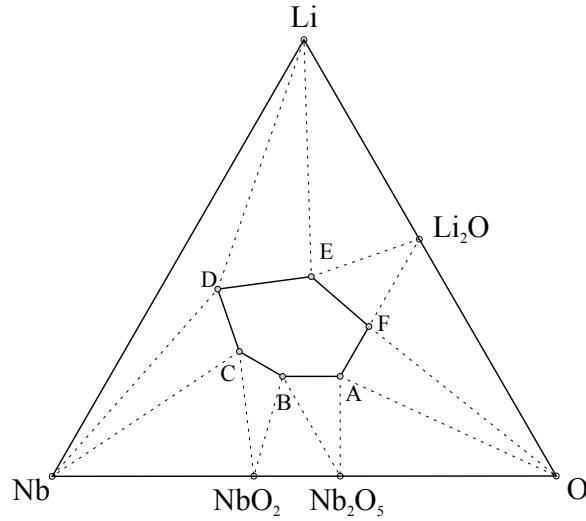
Figure 4.9: Schematic representation of the LiNbO₃ phase diagram with points (A-F) of interest labeled.

environment of commercially available crystals used in experiments.

Table 4.9: Total energy for each compound along with the chemical potential in each species at various points along the phase diagram for LiNbO₃

Condition	point	μ_{Li} (eV)	μ_{Nb} (eV)	μ_O (eV)
Stoich.		-8.79	-140.0	-427.52
$2\mu_{Nb} + 5\mu_O = \mu_{Nb_2O_5(bulk)}$,$\mu_O = \mu_{O(bulk)}$	A	-12.059	-155.378	-430.762
$2\mu_{Nb} + 5\mu_O = \mu_{Nb_2O_5(bulk)}$, $\mu_{Nb} + 2\mu_o = \mu_{NbO_2(bulk)}$	B	-9.171	-140.935	-436.539
$\mu_{Nb} + 2\mu O = \mu_{NbO_2(bulk)}$, $\mu_{Nb} = \mu_{Nb(bulk)}$	C	-10.205	-143.003	-435.505
$\mu_{Li} = \mu_{Li(bulk)}$, $\mu_{Nb} = \mu_{Nb(bulk)}$	D	-7.704	-143.003	-436.338
$2\mu_{Li} + \mu_O = \mu_{Li_2O(bulk)}$, $\mu_{Li} = \mu_{Li(bulk)}$	E	-7.704	-141.079	-436.980
$2\mu_{Li} + \mu_O = \mu_{Li_2O(bulk)}$, $\mu_O = \mu_{O(bulk)}$	F	-10.813	-156.624	-430.762

The chemical potentials reported in table 4.9 are broadly consistent with previous DFT based studies in LiNbO₃ . The exact numbers are not the same, as to be expected since it is a comparison between LCAO based DFT and PW based DFT[48] and the pseudopotentials differ. The trend however, is the same with defects demonstrating a similar trend. Another major difference from literature values could be due to the larger simulation cell sizes used here. Most DFT work performed on LiNbO₃ has utilized smaller system sizes (60-180 atoms, and 270 atoms)[13, 14, 19, 18]. Based on tests performed with the easiest defect to calculate, Li interstitials,

it became clear that the size of the system is required to be at least 270 atoms to eliminate influence of charge effects. Even larger system sizes are preferable which is the reason for the larger systems of 360 atoms used for E_{d} calculations.
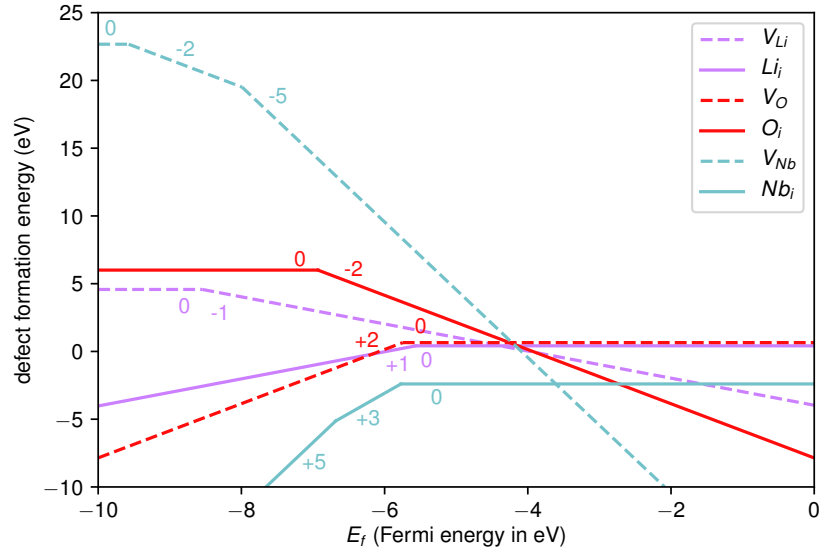
Figure 4.10: Defect formation energies for various types of defects in $LiNbO_3$ at the composition point B in figure figure 4.9

Charged defect formation energies reported in figure 4.10 shows the same trend as reported before. Larger simulation cells allows for the complete relaxation of systems (within a force tolerance of $1 \times 10^{-2} \frac{ev}{\text{Å}}$). The formation energies suggest that any Nb vacancy is energetically unfavorable, meaning it will either recombine or migrate through the system to form larger scale defects at defect sinks. Under irradiation, point defect production, further research needs to be conducted into the migration behavior of these defects to determine the defect configuration.

LiTaO₃

Often times work is done in parallel on $LiTaO_3$ and $LiNbO_3$ due to their compositional and chemical similarities. They are sometimes used in a mixture of the two compounds to tailor properties to the engineering task at hand. Because of this, the same procedures for determining defect formation in $LiNbO_3$ translate easily to $LiTaO_3$, with the exception that NbO_2 has no similar structure in the $LiTaO_3$ phase diagram (compare figure 4.9 to figure 4.11) so TaO is used instead.
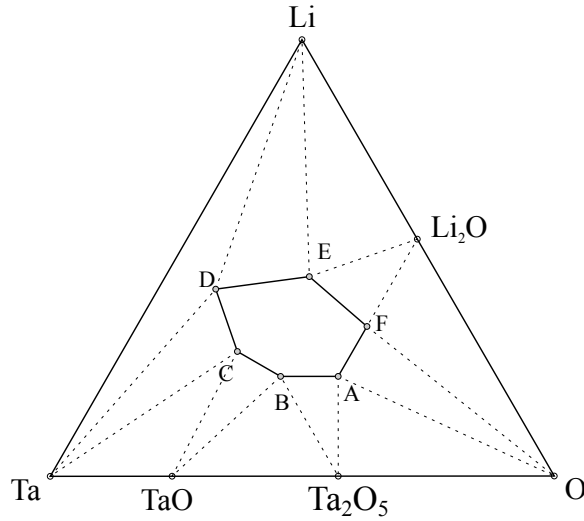
Figure 4.11: Schematic representation of the LiTaO$_3$ phase diagram with points (A-F) of interest labeled.

Table 4.10: Total energy for each compound along with the chemical potential in each species at various points along the phase diagram for LiTaO$_3$

Condition	point	μ_{Li} (eV)	μ_{Ta} (eV)	μ_O (eV)
$2\mu_{Ta} + 5\mu_O = \mu_{Ta_2O_5(bulk)}$,$\mu_O = \mu_{O(bulk)}$	A	-13.685	-149.034	-430.762
$2\mu_{Ta} + 5\mu_O = \mu_{Ta_2O_5(bulk)}$, $\mu_{Ta} + \mu_o = \mu_{TaO(bulk)}$	B	-11.365	-137.434	-435.402
$\mu_{Ta} + \mu_O = \mu_{TaO(bulk)}$, $\mu_{Ta} = \mu_{Ta(bulk)}$	C	-21.214	-142.358	-430.477
$\mu_{Li} = \mu_{Li(bulk)}$, $\mu_{Ta} = \mu_{Ta(bulk)}$	D	-7.704	-142.358	-434.981
$2\mu_{Li} + \mu_O = \mu_{Li_2O(bulk)}$, $\mu_{Li} = \mu_{Li(bulk)}$	E	-7.704	-136.361	-436.980
$2\mu_{Li} + \mu_O = \mu_{Li_2O(bulk)}$, $\mu_O = \mu_{O(bulk)}$	F	-10.813	-151.906	-430.762

Comparing tables 4.9 and 4.10 shows that the chemical potentials of both materials are very similar (with a few eV of each other). When the atoms are bonded to each other in a crystal lattice, it is expected that their valence electrons are similar if not nearly identical configurations. The main difference between the materials should come from the mass of the atoms involved.

From figure 4.12, it can be seen that, much like in LiNbO$_3$ in figure 4.10, the heavy cation (Ta) vacancies are energetically unfavorable. If these defects are produced during threshold displacement events, it suggests that they will either migrate or aggregate together in the structure contributing to larger scale structural changes. Longer time scales need to be probed for these interactions. As stated in the introduction, there are no suitable classical MD potentials for working

61
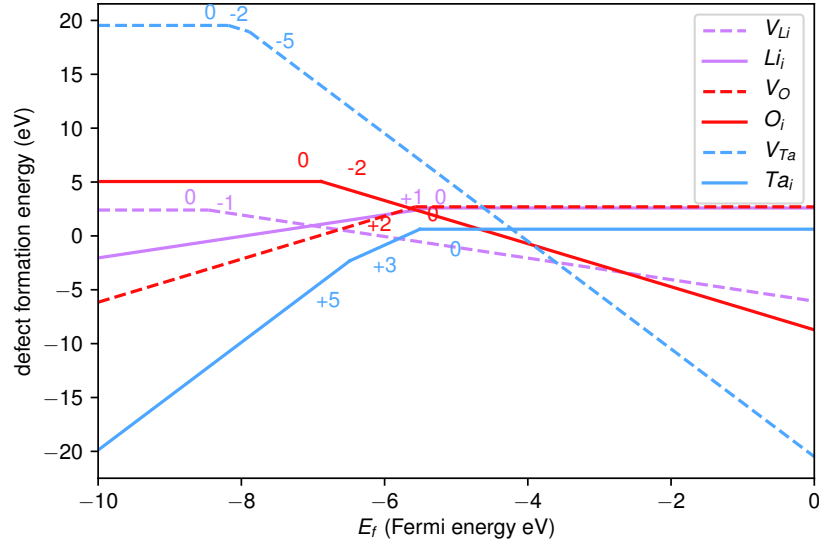
Figure 4.12: Defect formation energies for various types of defects in LiTaO$_3$ corresponding to composition point B in figure 4.11

with LiNbO$_3$ or LiTaO$_3$ defect structures. Either larger and longer scale *ab initio* calculations need to be made on specific defects (there have been recent advances improving the efficiency of the SIESTA code) or new MD potentials need to be developed. On the other hand, O^0 vacancies and neutral cation interstitials are much more energetically favorable, with a defect formation energy closer to 0 eV in both LiNbO$_3$ and LiTaO$_3$ as seen in figures 4.12 and 4.10.

4.5   Conclusion

LiNbO$_3$ and LiTaO$_3$ are tested in parallel to determine pseudopotential suitability through predicted material properties. Then the minimum energy configurations are used to calculate directionally dependent threshold displacement energies. The average values for LiNbO$_3$ are 29.7 eV for Li, 33.6 eV for Nb, and 22.4 eV for O. The average values for LiTaO$_3$ are 19.3 eV for Li, 24.4 eV for Ta and 36.79 eV for O. Broadly speaking, the cation defects are more easily produced in LiTaO$_3$ and the anion defects are more easily produced in LiNbO$_3$.

The resulting defect structures are then analyzed to determine their formation energies. The most energetically unfavorable defects produced are the neutrally charged large cation (Nb and

Ta) vacancies. O vacancies in both materials had low formation energies; the color centers from these vacancies in the intrinsic and irradiated materials obscure the observation of other defects experimentally. Overall, the interstitials prefer two orientations, one for cations and one for anions. Cations reside at the high symmetry site between coordinating octohedra on the c-axis. Anions form split interstitials, preferring to orient on one of the oxygen atoms between Li and the heavier cation. The split interstitial has not been previously well described in literature as most work has focused on oxygen vacancies and cation defect clusters.

Chapter 5

Conclusions

5.1 MgO

5.1.1 Material properties

Serving as a representative model material for working with the SIESTA code, MgO is used to determine the directionally dependent threshold displacement energies and defect properties of a system. The first step is to probe material properties like lattice constants, bulk modulus, and elastic constants, as these are reasonable indicators of the code's representation of inter-atomic forces. Once the results from these calculations are confirmed and compared with the results from experiment and other *ab initio* based calculations, the threshold displacement energies are calculated.

5.1.2 Threshold displacement events

The general trend in *ab intio* calculations is that they under estimate the threshold displacement energies in a system. The results for MgO demonstrate this trend quite clearly, in addition to confirming the varieties of defects formed. Only two types of interstitials are observed in all simulations. Either a body centered cation defect or a split anion defect along a face diagonal. Both types of defect have been reported in defect formation calculations, so no new structures are found in the MgO system.

5.1.3 Defects and defect properties

An analysis of all observed defect structures from the AIMD simulations showed good agreement with defect studies from other work on MgO. MgO is a good test system for these types of calculations because, at least for O defects, it prefers either a doubly charged defect or a neutral defect depending on the Fermi energy of the system. Mg defects are not well represented in DFT codes currently, but they are included to demonstrate the techniques used later on.

5.2 LiNbO$_3$ and LiTaO$_3$

5.2.1 Material properties

The more complicated structures of LiTaO$_3$ and LiNbO$_3$ require more in depth testing to determine the basic material properties. The mechanical properties provide a reasonable estimate for how the pseudopotentials represent forces between atoms. In particular the c_{11} and c_{12} directions are not particularly well represented in LiNbO$_3$ with values of 198 GPa and 55 GPa respectively. LiTaO$_3$ shows much better agreement with prior DFT and experimental work. The two materials also demonstrate very similar material properties; especially those based off the inter-atomic forces like lattice parameter, bulk modulus, and elastic properties.

5.2.2 Threshold displacement energies

The lowest energy required to displace an atom in any system is Li in LiTaO$_3$; it required only 6 eV to displace the atom from it's lattice site. The average threshold displacement energies determined from weighting based on directional multiplicity are in reasonable agreement with those used to calculate damage from TRIM and related methods. The highest value for E_d is 67 eV in LiNbO$_3$ along the c-axis. The major differences in the maximum and minimum E_d for the same PKA species in the two materials along different directions illustrates that the key difference is based on the interaction with the heavier cation (Nb or Ta).

5.2.3   Defects and defect properties

Cation defects produced agree well with the configurations reported previously, but anion defects are more complicated and prefer to form split interstitials. The cation interstitials where all located at the high symmetry site between the coordinating O octohedra. The anion defects preferred a split configuration with the two oxygen atoms aligning roughly $33.5°$ from the c-axis in most cases, slightly offset from the original lattice site. In total this provides for 6 possible defect configurations to describe the same type of split interstitial. Formation energies revealed that of all defects, Nb and Ta vacancies are extremely energetically unfavorable. The most favorable defects are O vacancies and Li interstitials in both materials, having formation energies close to zero. The result is that a high concentration of intrinsic O defects is expected (and observed), obscuring measurement of the other cation defects (particularly the color centers produced from cation defects). The cation vacancies tend to either migrate toward defect sinks, recombine, or form additional defect clusters (for instance, the reported Nb_{Li} antisite defect configurations). The larger defects that act as sinks for point defects could then become observable in the resulting post-irradiation material.

Bibliography

[1] Michel Freyss. Multiscale modelling of nuclear fuels under irradiation. *EPJ Web of Conferences*, 51:02003, 2013. ISSN 2100-014X. doi: 10.1051/epjconf/20135102003. URL http://www.epj-conferences.org/10.1051/epjconf/20135102003. xi, 5

[2] Robert M. Hanson. *Jmol – a paradigm shift in crystallographic visualization. Journal of Applied Crystallography*, 43(5):1250–1260, 2010. ISSN 0021-8898. xi, 7

[3] Pseudopotential, 2016. URL https://en.wikipedia.org/w/index.php?title=Pseudopotential&oldid=729396993. xi, 18

[4] B. Park, W. J. Weber, and L. R. Corrales. Molecular dynamics study of the threshold displacement energy in MgO. *Nuclear Instruments & Methods in Physics Research Section B-Beam Interactions with Materials and Atoms*, 166:357–363, 2000. ISSN 0168-583X. doi: 10.1016/S0168-583X(99)00694-1. xii, 33

[5] L. Kittiratanawasin, Roger Smith, B. P. Uberuaga, and K. E. Sickafus. Radiation damage and evolution of radiation-induced defects in er $_2$ o $_3$ bixbyite. *Journal of Physics: Condensed Matter*, 21(11):115403, 2009. ISSN 0953-8984, 1361-648X. doi: 10.1088/0953-8984/21/11/115403. xii, 33

[6] T. Sonoda, C. Kinoshita, and Y. Isobe. Static and dynamic properties of point defects in magnesia. *Annales De Physique*, 20(3):33–43, 1995. ISSN 0003-4169. xii, 33

[7] G. P. Pells. The temperature-dependence of the threshold displacement energy in MgO. *Radiation Effects and Defects in Solids*, 64(1):71–75, 1982. ISSN 1042-0150. xii, 33, 36

[8] Gary S. Was. *Fundamentals of Radiation Materials Science*. Springer Berlin Heidelberg, 2007. 2, 3

[9] R. S. Averback and T. Diaz Rubia. Displacement damage in irradiated metals and semiconductors. In Henry Ehrenreich Spaepen and Frans, editors, *Solid State Physics*, volume 51 of *Solid State PhysicsAdvances in Research and Applications*, pages 281–402. Academic Press, 1998. 3

[10] James F. Ziegler, M. D. Ziegler, and J. P. Biersack. SRIM - the stopping and range of ions in matter (2010). *Nuclear Instruments and Methods in Physics Research B*, 268:1818–1823, 2010. doi: 10.1016/j.nimb.2010.02.091. 3, 28

[11] J. B. Gibson, A. N. Goland, M. Milgram, and G. H. Vineyard. Dynamics of radiation damage. *Physical Review*, 120(4):1229–1253, 1960. 5, 11, 12

[12] L. Kittiratanawasin, Roger Smith, B. P. Uberuaga, and Kurt Sickafus. Displacement threshold and frenkel pair formation energy in ionic systems. *Nuclear Instruments & Methods in Physics Research Section B-Beam Interactions with Materials and Atoms*, 268(19):2901–2906, 2010. ISSN 0168-583X. 6

[13] Romel M Araujo, Krisztián Lengyel, Robert A Jackson, László Kovács, and Mário E G Valerio. A computational study of intrinsic and extrinsic defects in $LiNbO_3$. *Journal of Physics: Condensed Matter*, 19(4):046211, 2007. ISSN 0953-8984, 1361-648X. 6, 59

[14] Haixuan Xu, Donghwa Lee, Jun He, Susan B. Sinnott, Venkatraman Gopalan, Volkmar Dierolf, and Simon R. Phillpot. Stability of intrinsic defects and defect clusters in $LiNbO_3$ from density functional theory calculations. *Physical Review B*, 78(17), 2008. ISSN 1098-0121, 1550-235X. 6, 8, 43, 50, 59

[15] E. R. Hodgson and F. Agullo-Lopez. High-energy electron irradiation of stoichiometric $LiNbO_3$. *Journal of Physics: Condensed Matter*, 1(50):10015, 1989. ISSN 0953-8984. 6, 53

[16] F. Agulló-López, G. García, and J. Olivares. Theoretical modeling of swift-ion-beam amorphization: Application to $LiNbO_3$. *Nuclear Instruments and Methods in Physics Research Section B: Beam Interactions with Materials and Atoms*, 249(1):118–121, 2006. ISSN 0168583X. 6

[17] W. J. Weber, R. C. Ewing, C. R. A. Catlow, T. Diaz de la Rubia, L. W. Hobbs, C. Kinoshita, Hj. Matzke, A. T. Motta, M. Nastasi, E. K. H. Salje, E. R. Vance, and S. J. Zinkle. Radiation effects in crystalline ceramics for the immobilization of high-level nuclear waste and plutonium. *Journal of Materials Research*, 13(6):1434–1484, 1998. ISSN 2044-5326. 8

[18] Haixuan Xu, Donghwa Lee, Susan B Sinnott, Volkmar Dierolf, Venkatraman Gopalan, and Simon R Phillpot. Structure and diffusion of intrinsic defect complexes in $LiNbO_3$ from density functional theory calculations. *Journal of Physics: Condensed Matter*, 22(13): 135002, 2010. ISSN 0953-8984, 1361-648X. 8, 43, 50, 59

[19] Yanlu Li, W. G. Schmidt, and S. Sanna. Defect complexes in congruent $LiNbO_3$ and their optical signatures. *Physical Review B*, 91(17), 2015. ISSN 1098-0121, 1550-235X. 8, 59

[20] E. R. Hodgson and F. Agulló-López. Oxygen vacancy centres induced by electron irradiation in $LiNbO_3$. *Solid State Communications*, 64(6):965–968, 1987. ISSN 0038-1098. 10

[21] Frank Schrempel, Thomas Gischkat, Holger Hartung, Ernst Bernhard Kley, Werner Wesch, and Andreas Tünnermann. High aspect ratio microstructures in $LiNbO_3$ produced by ion beam enhanced etching. *MRS Online Proceedings Library Archive*, 908, 2005. ISSN 1946-4274, 0272-9172. 10

[22] P. Liu, Y. Zhang, H. Xue, K. Jin, M. L. Crespillo, X. Wang, and W. J. Weber. A coupled effect of nuclear and electronic energy loss on ion irradiation damage in lithium niobate. *Acta Materialia*, 105:429–437, 2016. ISSN 1359-6454. 10, 54

[23] Nicholas Metropolis, Arianna W. Rosenbluth, Marshall N. Rosenbluth, Augusta H. Teller, and Edward Teller. Equation of state calculations by fast computing machines. *The Journal of Chemical Physics*, 21(6):1087–1092, 1953. ISSN 0021-9606. doi: 10.1063/1.1699114. 11

[24] I. E. Fermi, P. Pasta, S. Ulam, and M. Tsingou. Studies of the nonlinear problems. Technical report, Los Alamos Scientific Lab., N. Mex., 1955. 11, 12

[25] B. J. Alder and T. E. Wainwright. Phase transition for a hard sphere system. *The Journal of Chemical Physics*, 27(5):1208–1209, 1957. ISSN 0021-9606. doi: 10.1063/1.1743957. 11

[26] A. Rahman. Correlations in the motion of atoms in liquid argon. *Physical Review*, 136(2): A405–A411, 1964. 11, 12

[27] Aneesur Rahman and Frank H. Stillinger. Molecular dynamics study of liquid water. *The Journal of Chemical Physics*, 55(7):3336–3359, 1971. ISSN 0021-9606. doi: 10.1063/1. 1676585. 11

[28] I. R. McDonald. NpT-ensemble monte carlo calculations for binary liquid mixtures. *Molecular Physics*, 23(1):41–58, 1972. 11

[29] Hans C. Andersen. Molecular dynamics simulations at constant pressure and/or temperature. *The Journal of Chemical Physics*, 72(4):2384–2393, 1980. ISSN 0021-9606. doi: 10.1063/1.439486. 11

[30] M. Parrinello and A. Rahman. Crystal structure and pair potentials: A molecular-dynamics study. *Physical Review Letters*, 45(14):1196–1199, 1980. 11, 13

[31] M. Parrinello and A. Rahman. Polymorphic transitions in single crystals: A new molecular dynamics method. *Journal of Applied Physics*, 52(12):7182–7190, 1981. ISSN 0021-8979. doi: 10.1063/1.328693. 11

[32] R. Car and M. Parrinello. Unified approach for molecular dynamics and density-functional theory. *Physical Review Letters*, 55(22):2471–2474, 1985. 11, 13, 15, 20

[33] Michael P. Allen. *Introduction to Molecular Dynamics Simulation*. Number 23 in NIC series. NIC, 2004. ISBN 978-3-00-012641-3. 14

[34] Kieron Burke and Lucas O. Wagner. DFT in a nutshell. *International Journal of Quantum Chemistry*, 113(2):96–101, 2013. ISSN 1097-461X. 14, 15

[35] D. R. Hartree. The wave mechanics of an atom with a non-coulomb central field. part i. theory and methods. *Mathematical Proceedings of the Cambridge Philosophical Society*, 24 (1):89–110, 1928. ISSN 1469-8064, 0305-0041. doi: 10.1017/S0305004100011919. 15

[36] J. C. Slater. A simplification of the hartree-fock method. *Physical Review*, 81(3):385–390, 1951. doi: 10.1103/PhysRev.81.385. 15

[37] George W. Pratt. Wave functions and energy levels for Cu as found by the slater approximation to the hartree-fock equations. *Physical Review*, 88(6):1217–1224, 1952. doi: 10.1103/PhysRev.88.1217. 15

[38] P. Hohenberg and W. Kohn. Inhomogeneous electron gas. *Physical Review*, 136(3):B864–B871, 1964. doi: 10.1103/PhysRev.136.B864. 15

[39] W. Kohn and L. J. Sham. Self-consistent equations including exchange and correlation effects. *Physical Review*, 140(4):A1133–A1138, 1965. doi: 10.1103/PhysRev.140.A1133. 15

[40] B. Y. Tong and L. J. Sham. Application of a self-consistent scheme including exchange and correlation effects to atoms. *Physical Review*, 144(1):1–4, 1966. doi: 10.1103/PhysRev.144. 1. 15

[41] M. Born and R. Oppenheimer. Zur quantentheorie der molekeln. *Annalen der Physik*, 389: 457–484, 1927. ISSN 0003-3804. 15

[42] G. Kresse and J. Furthmüller. Efficient iterative schemes for ab initio total-energy calculations using a plane-wave basis set. *Physical Review B*, 54(16):11169–11186, 1996. doi: 10.1103/ PhysRevB.54.11169. 17

[43] J. M. Soler, E. Artacho, J. D. Gale, A. Garcia, J. Junquera, P. Ordejon, and D. Sanchez-Portal. The SIESTA method for ab initio order-n materials simulation. *Journal of Physics-Condensed Matter*, 14(11):2745–2779, 2002. ISSN 0953-8984. 17, 18, 20, 23, 24, 42, 43

[44] X. Gonze, J. M. Beuken, R. Caracas, F. Detraux, M. Fuchs, G. M. Rignanese, L. Sindic, M. Verstraete, G. Zerah, F. Jollet, M. Torrent, A. Roy, M. Mikami, Ph. Ghosez, J. Y. Raty, and D. C. Allan. First-principles computation of material properties: the ABINIT software project. *Computational Materials Science*, 25(3):478–492, 2002. ISSN 0927-0256. doi: 10.1016/S0927-0256(02)00325-7. 17

[45] Stewart J. Clark, Matthew D. Segall, Chris J. Pickard, Phil J. Hasnip, Matt I. J. Probert, Keith Refson, and Mike C. Payne. First principles methods using CASTEP. *Zeitschrift für Kristallographie - Crystalline Materials*, 220(5):567–570, 2009. ISSN 2196-7105. doi: 10.1524/zkri.220.5.567.65075. 17

[46] Paolo Giannozzi, Stefano Baroni, Nicola Bonini, Matteo Calandra, Roberto Car, Carlo Cavazzoni, Davide Ceresoli, Guido L. Chiarotti, Matteo Cococcioni, Ismaila Dabo, Andrea Dal Corso, Stefano de Gironcoli, Stefano Fabris, Guido Fratesi, Ralph Gebauer, Uwe Gerstmann, Christos Gougoussis, Anton Kokalj, Michele Lazzeri, Layla Martin-Samos, Nicola Marzari, Francesco Mauri, Riccardo Mazzarello, Stefano Paolini, Alfredo Pasquarello,

Lorenzo Paulatto, Carlo Sbraccia, Sandro Scandolo, Gabriele Sclauzero, Ari P. Seitsonen, Alexander Smogunov, Paolo Umari, and Renata M. Wentzcovitch. QUANTUM ESPRESSO: a modular and open-source software project for quantum simulations of materials. *Journal of Physics: Condensed Matter*, 21(39):395502, 2009. ISSN 0953-8984. doi: 10.1088/ 0953-8984/21/39/395502. 17

[47] Karlheinz Schwarz and Peter Blaha. Solid state calculations using WIEN2k. *Computational Materials Science*, 28(2):259–273, 2003. ISSN 0927-0256. doi: 10.1016/S0927-0256(03) 00112-5. 17

[48] Pablo Rivero, Víctor Manuel García-Suárez, David Pereñiguez, Kainen Utt, Yurong Yang, Laurent Bellaiche, Kyungwha Park, Jaime Ferrer, and Salvador Barraza-Lopez. Systematic pseudopotentials from reference eigenvalue sets for DFT calculations. *Computational Materials Science*, 98:372–389, 2015. ISSN 0927-0256. 18, 43, 59

[49] S.R. Bahn and K.W. Jacobsen. An object-oriented scripting interface to a legacy electronic structure code. *Computing in Science & Engineering*, 4(3):56–66, 2002. ISSN 15219615. 20

[50] B. Liu, H. Y. Xiao, Y. Zhang, and W. J. Weber. Ab initio molecular dynamics simulations of overlapping recoil events in ThO$_2$. *Journal of Physics-Condensed Matter*, 25(39):395004, 2013. ISSN 0953-8984. 20, 27

[51] B. Liu, H. Y. Xiao, Y. Zhang, D. S. Aidhy, and W. J. Weber. Ab initio molecular dynamics simulations of threshold displacement energies in SrTiO$_3$. *Journal of Physics-Condensed Matter*, 25(48):485003, 2013. ISSN 0953-8984. 20, 40

[52] E. Holmström, A. Kuronen, and K. Nordlund. Threshold defect production in silicon determined by density functional theory molecular dynamics simulations. *Physical Review B*, 78(4):045202, 2008. doi: 10.1103/PhysRevB.78.045202. 20

[53] F. Gao and W. J. Weber. Cascade overlap and amorphization in 3C-SiC: Defect accumulation, topological features, and disordering. *Physical Review B*, 66(2):024106, 2002. ISSN 1098- 0121. 23

[54] N. Troullier and Jl Martins. Efficient pseudopotentials for plane-wave calculations. *Physical Review B*, 43(3):1993–2006, 1991. ISSN 0163-1829. 24

[55] L. Kleinman and Dm Bylander. Efficacious form for model pseudopotentials. *Physical Review Letters*, 48(20):1425–1428, 1982. ISSN 0031-9007. doi: 10.1103/PhysRevLett.48.1425. 24

[56] J. P. Perdew, K. Burke, and M. Ernzerhof. Generalized gradient approximation made simple. *Physical Review Letters*, 77(18):3865–3868, 1996. ISSN 0031-9007. 24

[57] Francis Birch. Finite elastic strain of cubic crystals. *Physical Review*, 71(11):809–824, 1947. 24, 25

[58] F. D. Murnaghan. The compressibility of media under extreme pressures. *Proceedings of the National Academy of Sciences of the United States of America*, 30(9):244–247, 1944. ISSN 0027-8424. 24, 25

[59] Maarten de Jong, Wei Chen, Thomas Angsten, Anubhav Jain, Randy Notestine, Anthony Gamst, Marcel Sluiter, Chaitanya Krishna Ande, Sybrand van der Zwaag, Jose J Plata, Cormac Toher, Stefano Curtarolo, Gerbrand Ceder, Kristin A. Persson, and Mark Asta. Charting the complete elastic properties of inorganic crystalline compounds. *Scientific Data*, 2:150009, 2015. ISSN 2052-4463. 26, 45, 51

[60] Shyue Ping Ong, William Davidson Richards, Anubhav Jain, Geoffroy Hautier, Michael Kocher, Shreyas Cholia, Dan Gunter, Vincent L. Chevrier, Kristin A. Persson, and Gerbrand Ceder. Python materials genomics (pymatgen): A robust, open-source python library for materials analysis. *Computational Materials Science*, 68:314–319, 2013. ISSN 0927-0256. 26

[61] S. J. Zinkle and C. Kinoshita. Defect production in ceramics. *Journal of Nuclear Materials*, 251:200–217, 1997. ISSN 0022-3115. 28, 36

[62] R. M. Hazen. Effects of temperature and pressure on cell dimension and x-ray temperature factors of periclase. *American Mineralogist*, 61(3):266–271, 1976. ISSN 0003-004X. 30

[63] S. Sasaki, K. Fujino, and Y. Takeuchi. X-ray determination of electron-density distributions in oxides, MgO, MnO, CoO, and NiO, and atomic scattering factors of their constituent atoms. *Proceedings of the Japan Academy Series B-Physical and Biological Sciences*, 55(2):43–48, 1979. ISSN 0386-2208. doi: 10.2183/pjab.55.43. 30

[64] V. G. Tsirelson, A. S. Avilov, Y. A. Abramov, E. L. Belokoneva, R. Kitaneh, and D. Feil. X-ray and electron diffraction study of MgO. *Acta Crystallographica Section B-Structural Science*, 54:8–17, 1998. ISSN 0108-7681. doi: 10.1107/S0108768197008963. 30

[65] P. Karen, A. Kjekshus, Q. Huang, and V. L. Karen. The crystal structure of magnesium dicarbide. *Journal of Alloys and Compounds*, 282(1):72–75, 1999. ISSN 0925-8388. doi: 10.1016/S0925-8388(98)00828-7. 30

[66] M. Boiocchi, F. Caucia, M. Merli, D. Prella, and L. Ungaretti. Crystal-chemical reasons for the immiscibility of periclase and wustite under lithospheric P, T conditions. *European Journal of Mineralogy*, 13(5):871–881, 2001. ISSN 0935-1221. doi: 10.1127/0935-1221/2001/0013/0871. 30

[67] D. G. Isaak, O. L. Anderson, and T. Goto. Measured elastic-moduli of single-crystal MgO up to 1800-k. *Physics and Chemistry of Minerals*, 16(7):704–713, 1989. ISSN 0342-1791. 30

[68] O. L. Anderson and C. P. Andrea. Pressure derivatives of elastic constants of single-crystal MgO at 23 degrees and -195.8 degrees c. *Journal of the American Ceramic Society*, 49(8): 404–&, 1966. ISSN 0002-7820. doi: 10.1111/j.1151-2916.1966.tb15405.x. 30

[69] H. K. Mao and P. M. Bell. Equations of state of MgO and epsilon-Fe under static pressure conditions. *Journal of Geophysical Research*, 84:4533–4536, 1979. ISSN 0148-0227. doi: 10.1029/JB084iB09p04533. 30

[70] M. J. Mehl, R. E. Cohen, and H. Krakauer. Linearized augmented plane-wave electronic-structure calculations for MgO and CaO. *Journal of Geophysical Research-Solid Earth and Planets*, 93:8009–, 1988. ISSN 0148-0227. doi: 10.1029/JB093iB07p08009. 30

[71] J. E. Jaffe, J. A. Snyder, Z. J. Lin, and A. C. Hess. LDA and GGA calculations for high-pressure phase transitions in ZnO and MgO. *Physical Review B*, 62(3):1660–1665, 2000. ISSN 1098-0121. doi: 10.1103/PhysRevB.62.1660. 30

[72] K. Marklund and S. A. Mahmoud. Elastic constants of magnesium oxide. *Physica Scripta*, 3 (2):75, 1971. ISSN 1402-4896. 31

[73] E. H. Bogardus. Third☐order elastic constants of ge, MgO, and fused SiO_2. *Journal of Applied Physics*, 36(8):2504–2513, 1965. ISSN 0021-8979. 31

[74] H. Baltache, R. Khenata, M. Sahnoun, M. Driz, B. Abbar, and B. Bouhafs. Full potential calculation of structural, electronic and elastic properties of alkaline earth oxides MgO, CaO and SrO. *Physica B: Condensed Matter*, 344(1):334–342, 2004. ISSN 0921-4526. 31

[75] F Marinelli and A Lichanot. Elastic constants and electronic structure of alkaline-earth chalcogenides. performances of various hamiltonians. *Chemical Physics Letters*, 367(3):430–438, 2003. ISSN 0009-2614. 31

[76] J. Mulroue and D. M. Duffy. An ab initio study of the effect of charge localization on oxygen defect formation and migration energies in magnesium oxide. *Proceedings of the Royal Society a-Mathematical Physical and Engineering Sciences*, 467(2131):2054–2065, 2011. ISSN 1364-5021. 36, 39

[77] T. Brudevoll, E. A. Kotomin, and N. E. Christensen. Interstitial-oxygen-atom diffusion in MgO. *Physical Review B*, 53(12):7731–7735, 1996. ISSN 0163-1829. doi: 10.1103/ PhysRevB.53.7731. 36

[78] B. P. Uberuaga, R. Smith, A. R. Cleave, G. Henkelman, R. W. Grimes, A. F. Voter, and K. E. Sickafus. Dynamical simulations of radiation damage and defect mobility in MgO. *Physical Review B*, 71(10):104102, 2005. 36

[79] H. Y. Xiao, Fei Gao, X. T. Zu, and W. J. Weber. Threshold displacement energy in GaN: Ab initio molecular dynamics study. *Journal of Applied Physics*, 105(12):123527, 2009. ISSN 00218979. 36

[80] H. Y. Xiao, F. Gao, and W. J. Weber. Threshold displacement energies and defect formation energies in $Y_2Ti_2O_7$. *Journal of Physics-Condensed Matter*, 22(41):415801, 2010. ISSN 0953-8984. doi: 10.1088/0953-8984/22/41/415801. 36

[81] X. J. Wang, H. Y. Xiao, X. T. Zu, Y. Zhang, and W. J. Weber. Ab initio molecular dynamics simulations of ion-solid interactions in $Gd_2Zr_2O_7$ and $Gd_2Ti_2O_7$. *Journal of Materials Chemistry C*, 1(8):1665–1673, 2013. ISSN 2050-7526. doi: 10.1039/c2tc00192f. 36

[82] R. Hsu, E. N. Maslen, D. du Boulay, and N. Ishizawa. Synchrotron X-ray Studies of $LiNbO_3$ and $LiTaO_3$. *Acta Crystallographica Section B Structural Science*, 53(3):420–428, 1997. ISSN 01087681. doi: 10.1107/S010876819600777X. 50

[83] Jin Yang, Jianping Long, and Lijun Yang. First-principles investigations of the physical properties of lithium niobate and lithium tantalate. *Physica B: Condensed Matter*, 425:12–16, 2013. ISSN 0921-4526. 50, 51

[84] Y. Nakanishi, H. Mizota, Y. Ito, M. Takano, S. Fukao, S. Yoshikado, K. Ohyama, K. Yamada, and S. Fukushima. Relation between x-ray emission mechanism and crystal structure in $LiNbO_3$. *Physica Scripta*, 73(5):471, 2006. ISSN 1402-4896. doi: 10.1088/0031-8949/73/5/010. 50

[85] G. Kovacs, M. Anhorn, H. E. Engan, G. Visintini, and C. C. W. Ruppel. Improved material constants for $LiNbO_3$ and $LiTaO_3$. In *Ultrasonics Symposium, 1990. Proceedings., IEEE 1990*, pages 435–438 vol.1, 1990. 51

[86] Shaoxin Feng, Qinghua Jin, Baohui Li, Zhenya Guo, and Datong Ding. Empirical calculations of the formation energies of intrinsic defects in lithium niobate. *arXiv preprint cond-mat/0012499*, 2000. 51

Vita

Benjamin Petersen was born in Knoxville, TN, and grew up in and around the Knoxville area. He had wanted to be an engineer since he figured out what the word meant when he was four years old. Since then he graduated high school and knew exactly what he wanted to do: get a degree in engineering. In high school he began to be involved with the University of Tennessee Materials Science and Engineering department where he would later be accepted as a Chancellor's Scholar for an undergraduate degree. At the University of Tennessee, in 2012 as he was working on his undergraduate degree, he was offered a position as a doctoral student working on radiation effects in materials with the UT Ion Beam Materials Laboratory. While there, he became fascinated with utilizing computational techniques to study material properties and relating them to experimental observations.